Magnetic Shim Coils for Zeeman Splitting and Ambient Field Homogeneity in the JILA eEDM Generation III Experiment

Author: Gus Santaella

Thesis advisor: Eric Cornell (JILA/Physics)

Honors representative: Jun Ye (JILA/Physics)

Outside reader: Zachory Berta-Thompson (Astrophysical and Planetary Sciences)

A thesis presented for partial fulfilment of the degree of

Bachelor of Arts in Physics with Honors Distinction

JILA/Physics Department

University of Colorado Boulder

Boulder, CO, United States of America

March 28th 2022

To my mom and dad. And to those that dare to dream.

Acknowledgements

I'm of the belief that one is nothing without the people behind them. I am truly thankful for the people that are around me now, and it is clear to me that the work done on this thesis would not have been possible without them. I'll be as brief as I can, but I'd like to use this space to acknowledge them all.

First, I'd like to acknowledge my closest friends at CU Boulder: Peter Lande, Shreyas Kadekodi, Kyle Pfromer, Nick Lumiere, Saurabh Totey, Ethan Olander, Jishnu Raychaudhuri, Ravin Chowdhury, Phoebe Rudnick, Rex Planalp, Karin Roley, Teddy Gonzalez, and Sanjay Kumar Keshava. Thank you all for your friendship and for getting through the communal struggle of college with me.

Over in Mexico, I'd like to acknowledge my entire family and my friends: Anahí Lima, Regina de Orta Pando, Miguel Bahena, Cornelio Menendez, Dany Gomezpedroso, Javier González, Sebastian Huitron, Sharif Rod, Sergio Carrillo, Dany Carrillo, Andree González, Aldo García, Jacques de Botton, and Toño Crespo. Thank you all for your friendship and support despite the years and despite the distance.

In the machine shop at JILA, I'd like to acknowledge Adam Elizey, James Uhrich, Calvin Schwadron, and, most importantly, Hans Green for all their support in guiding me to become a better machinist.

In the Cornell group, I'd like to acknowledge the entire eEDM generation III team: Kia Boon Ng, Noah Schlossberger, Anzhou Wang, Sun Yool Park, Ben Hunt, and Antonio Vigil. Also, I'd like to acknowledge Trevor Wright and Luke Caldwell over in Generation II and Michael Van De Graff over in JRIB.

Of these people, I'd like to make special mentions to Noah Schlossberger for his

mentorship and kindness in guiding me through the various sections of this project, especially throughout the harsh building process, to Kia Boon Ng for his aid in helping me understand the theory behind the JILA eEDM generation III experiment and physics in general, especially throughout the theoretical and computational aspects of this project, and to Antonio Vigil for all his generous and extremely helpful advice and guidance.

Lastly, I'd like to thank Eric Cornell and Jun Ye for giving me the privilege to work under them and their amazing research group throughout these years and for all the support in this project. Every single day I spent on this group I felt like I learned something new, and I always felt rewarded by your teachings. Through all the highs and lows, I learned a ton of amazing things that have helped me become a better physicist and, most importantly, a better and more confident person. To say the least, I am forever in debt with you all for this amazing experience.

Contents

I

1 Introduction

1.1 The Standard Model, the eEDM, and their implications on physics

The standard model of particle physics is a theory that attempts to combine three of the four fundamental forces (electromagnetic, weak interaction and strong interaction, not accounting for gravity) into a single frame of reference to explain elementary particles. [3]

While the model has proven to be successful at giving very accurate experimental predictions, some of which have given rise to some relevant discoveries in the fields of atomic, molecular, and optical physics over the past century or so, it relies on various assumptions and omissions that simplify the model at the expense of leaving certain physical phenomena unexplained. This potentially limits the growth of the field and maybe even prevents the discovery of new realms of physics beyond the standard model. [3]

One such prediction that the electron electric dipole moment (eEDM), which is essentially the measure of the distance between the center of charge and the center of mass of the electron times its charge, has a very small value of about 10^{-38} $e \cdot cm$ at most.

Experimentally measured values, however, may indicate a discrepancy in the upper bound of this prediction, which is why measuring it is a means of testing the standard model of physics. Moreover, finding a finite, non-zero eEDM larger than 10^{-38} $e \cdot cm$ is a violation of the standard model which implies a few things. First

of all, it tells us about an otherwise unpredicted charge parity (CP) violation within the inner structure of the electron, and second it tells us about time (T) violations as well.

Considering all of the above, if an experimentally measured eEDM is found to be considerably larger than what the standard model prediction tells us, this would imply that there is new, beyond the standard model physics, potentially opening up the way for a new branch of studies within the field.

Nowadays, there are multiple collaborations trying to experimentally determine the most precise measurement of the eEDM, including the JILA eEDM collaboration led by Eric Cornell and Jun Ye at the University of Colorado - Boulder. During the first two generations of the experiment, colloquially known as the Generation I (2017, final eEDM limit of $< 1.3 \times 10^{-28} \ e \cdot cm$ in HfF$^+$ ions [1]) and Generation II (2022, which is predicted to give a final eEDM sensitivity of about 10^{-29}, also in HfF$^+$ ions), the collaboration has sought to improve its methodology and experimental techniques.
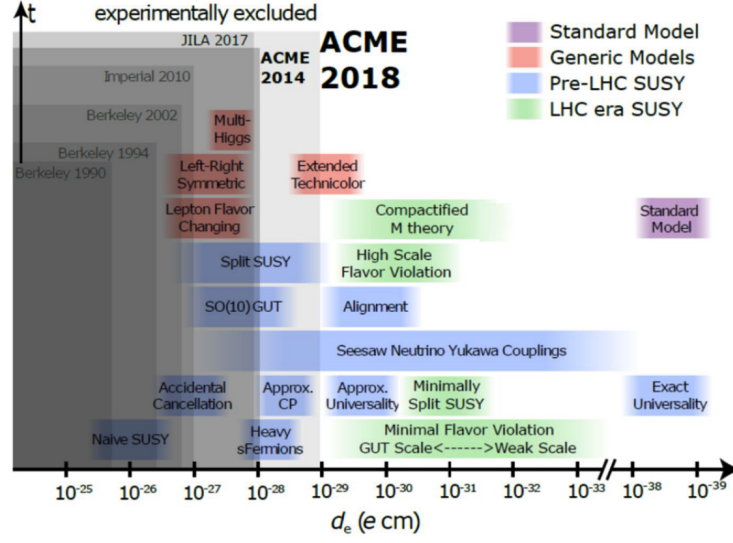
Figure 1.1: This image shows the progress in the search for the eEDM. Visible are the the ACME collaboration's (Harvard/Chicago/Northwestern) generation I (2014) and generation 2 (2018) results, along with the JILA eEDM collaboration's 2017 Generation I result. Note how both of these numbers are orders of magnitude larger than the standard model prediction, which is of than 10^{-38} $e \cdot cm$ or less. Image credits: Gerald Gabrielse (ACME)

3

1.2 The Generation III experiment at JILA
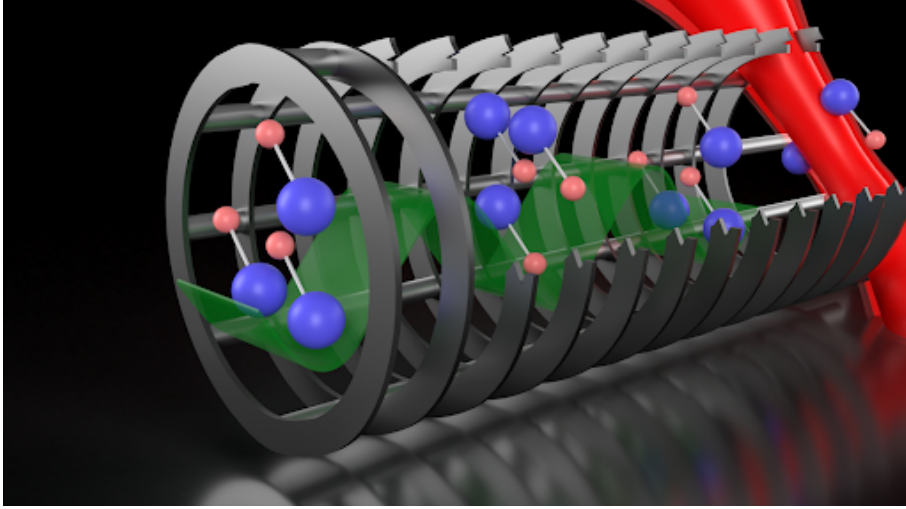
Figure 1.2: An artist's depiction of the Generation III "Bucket Brigade" setup, in which the tube serving as the conveyor belt can be appreciated carrying the ionized ThF^+ molecules along its axis. Image credits: Noah Schlossberger.

Working upon the legacy of the Generation I and Generation II experiments, the JILA eEDM collaboration is looking to continue its efforts to experimentally measure the best possible measurement of the eEDM. Because of this, the idea of the generation III experiment was conceived.

As opposed to the generation I and generation II experiments, both which used HfF^+ ions, the generation III experiment will use thorium fluoride ions (ThF^+). This switch was necessary given that the electric field between the Th and F atoms (referred to as E_{eff}) in ThF^+ is 1.5 times stronger than that between Hf and F atoms in HfF^+. A vast amount of research time was spent doing spectroscopy on ThF^+ to better understand it, given that it is was previously a relatively novel and not well-characterized species. Refer to [2] and [4] for more information on ThF^+.

4

The experimental setup of the Generation III experiment, colloquially known as the Bucket Brigade, is essentially a very long conveyor belt of Paul traps. The ThF$^+$ molecules are first ionized using various YAG and ECDL lasers to achieve the desired quantum transitions, then they're sent down the conveyor of the Bucket Brigade, then they're dissociated, and the fluoride atoms from the dissociated ions hit a screen in front of an MCP camera which captures the data. Here, the dissociated ions form two blobs each corresponding to the orientation of the thorium in the molecule at the time of dissociation.

Figure 1.3: The full setup of the Generation III Bucket Brigade. The state preparation procedure, the conveyor belt, and the ion dissociation procedure can all be appreciated in the image. Image credits: Kia Boon Ng, Sun Yool Park, Noah Schlossberger, et al.

This data can then be translated as resonance curves, forming a doublet of Gaussians as seen in figure 1.4. Each Gaussian in the doublet corresponds to two different resonances: one corresponding to the upper doublet states of ThF$^+$ and the other one corresponding and lower doublet states of ThF$^+$ (as seen in the energy diagram

from figure 2.2). These resonances are essential in determining the eEDM, because so it happens that the separation between the peaks of each Gaussian is equal to $2d_e E_{eff}$, where d_e is the eEDM. (figure 1.4)

1.2.1 The statistical motives behind the Generation III experiment

In essence, the motive behind why we want to build this rather elaborate setup, complex in both theory and practice, reduces to a desire to maximize very simple statistical concepts in our favor to give us as good an eEDM measurement as possible. This is because the shape of the Gaussians changes drastically given three main factors: the count rate (the number of "measurements" you obtain), the coherence time (how long you have ionized molecules in a stable state to be able to interrogate them), and the size of the molecular electric field between the Th and F atoms in ThF$^+$ felt by the electron spin (E_{eff}).

Essentially, the larger the count rate you have, the smoother your resonance curves are. The longer the coherence time is, the sharper and more defined the resonance peaks are. And finally, the larger E_{eff} is, the more separated the each resonance curve is from one another. A visual representation of these statements can be found in figure 1.4. It must be noted that, in the real experiment, the resonance curves forming these two Gaussians are not as separated as depicted in this figure, which is purposefully exaggerated. Instead, the real resonance curves almost overlap with one another, with the separation between their peaks being very small.
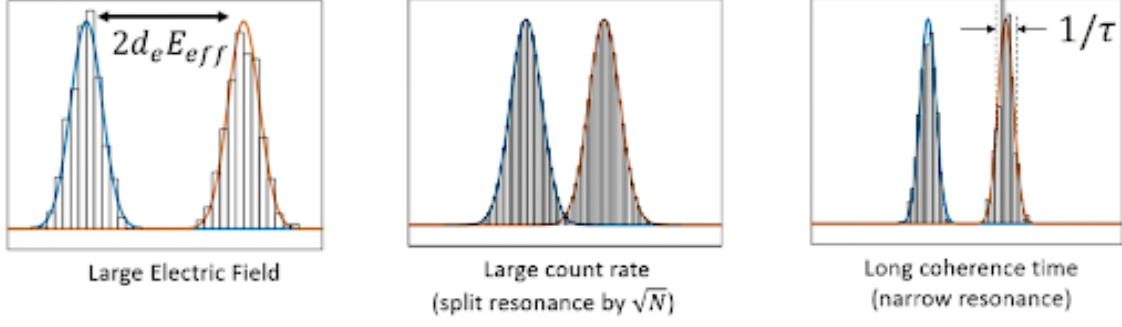
Figure 1.4: The larger the count rate you have, the smoother your resonance is. The longer the coherence time is, the sharper and more defined the resonance peaks are, and the larger E_{eff} is, the more separated the each resonance is from one another. Image credits: Kia Boon Ng, Sun Yool Park, Noah Schlossberger, et al.

Hence, the Generation III experiment's Bucket Brigade directly affects all of these factors by allowing us to 1) run a large amount of experiments at the same time to maximize the count rate, given its large capacity to have multiple Paul traps running along its axis, 2) give us a large coherence time, given the many techniques being put in place to keep the ions in a stable environment (hopefully for about 20 seconds, realistically to about 8 seconds), and 3) have a molecule like ThF^+ with an E_{eff} large enough to produce a dectectable signal for the eEDM.

Before building the complete experiment, however, we are interested in the building just half of it to do tests and make sense of how much true coherence time we'll obtain from the setup once the full Bucket Brigade is built. This reduced setup is colloquially called the "Baby Bucket", and in it the ions will be ionized, go down a 1 meter long cryogenically-cooled and insulated tube and come back down the same tube, and then be dissociated into the MCP camera. This is depicted in figure 1.5.

7
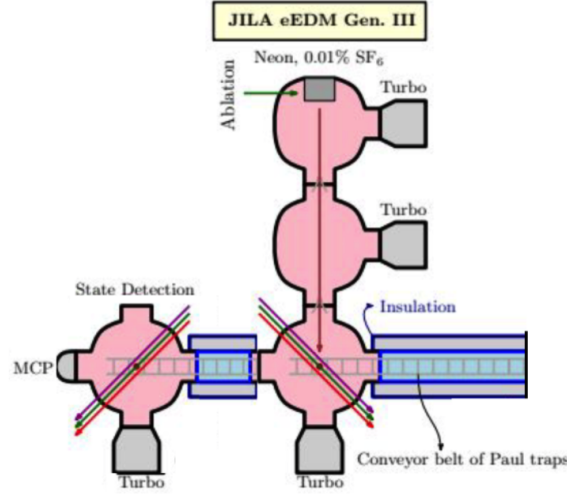
Figure 1.5: The Baby Bucket setup. Image credits: Kia Boon Ng, Sun Yool Park, Noah Schlossberger, et al.

For more information work being done on the Generation III experiment, refer to its corresponding papers [2] and [4] found in the bibliography.

1.2.2 Trapping ThF$^+$ with a rotating electric field E_{rot} induced by electrodes
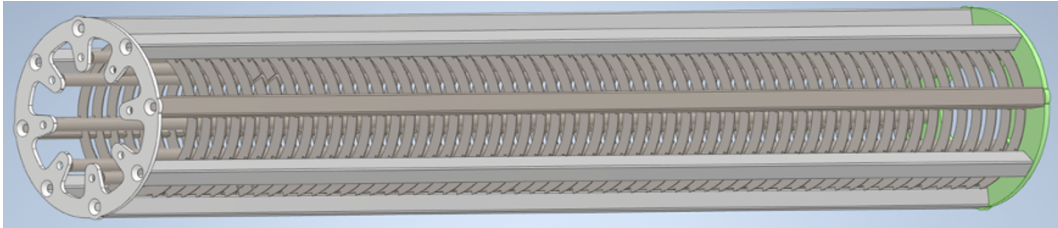
Figure 1.6: A CAD model of the prototype of the electrodes in the full Bucket Brigade and the Baby Bucket Brigade. Image credits: Anzhou Wang, Kia Boon Ng, et al.

One of the marquee features of the Generation III experiment, as a whole, is the use of various long electrode rods placed radially along the axis of the trap that generate a rotating electric field.

To make sense of the purpose of the electrodes, think of a dipolar molecule like ThF$^+$ in the presence of an external, static electric field. Due to its net positive charge, it will want to escape the potential in the presence of the electric field given the electric force $\vec{F} = q\vec{E_{ext}}$ (see figure 1.7). This is of course, inconvenient, given that you want to have the ions stay in place for a long period of coherence to interrogate them.
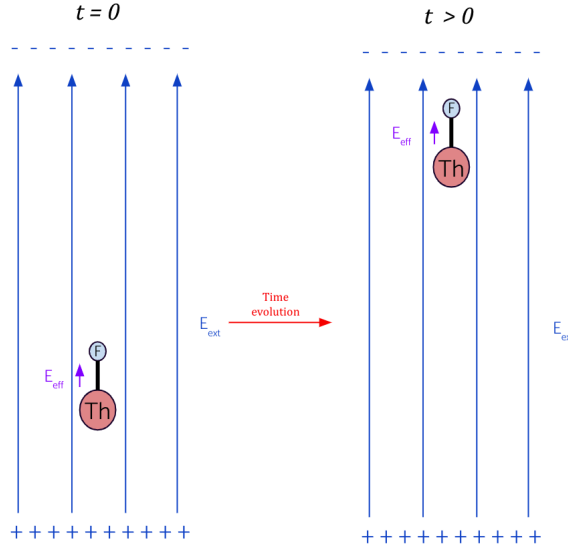
Figure 1.7: Depiction of a ThF$^+$ molecule in a static electric field. Given the the electric force pushing it towards the negative potential, the molecule swiftly flies away.

We can change this, however, by letting the external electric field E_{ext} rotate as opposed to being static. Doing so results prevents the molecule from flying away

(figure 1.8), staying relatively "trapped" and forming a circular trace with radius equal to r_{rot} along the $\hat{x}$-$\hat{y}$ plane of the trap (figure 1.9).
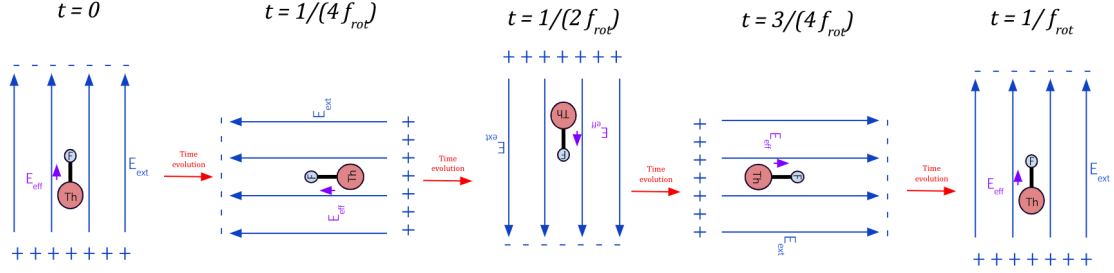
Figure 1.8: Depiction of a ThF$^+$ molecule in a rotating electric field. If designed correctly, the rotating electric force over a full period does not cause the molecule to fly away
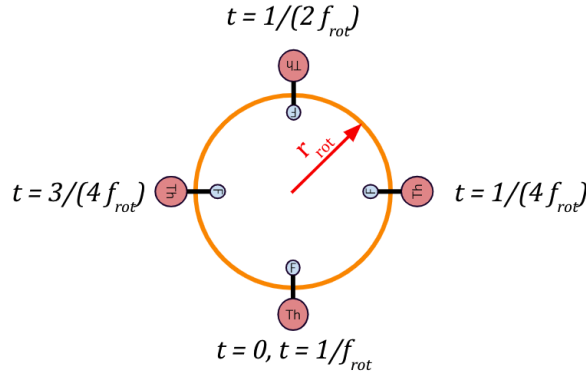
Figure 1.9: Circular trace of radius r_{rot} formed by a molecule in a rotating electric field over a full period

In the Bucket Brigade, this rotating electric field is called E_{rot}, which is the quantization axis of the ThF$^+$ ions, and it takes the form:

10

$$\vec{E_{rot}} = \epsilon_{rot} \begin{bmatrix} cos(\omega_{rot}\, t) \\ sin(\omega_{rot}\, t) \\ 0 \end{bmatrix} \tag{1.1}$$

where ϵ_{rot} is the amplitude of the electric field, and $\omega_{rot} = 2\,\pi\,f_{rot}$ is the angular frequency of rotation.

2   Scientific considerations relevant to this project

2.1   The science transition in ThF$^+$ and its relation to measuring the eEDM

Being a molecule, the quantum energy states in ThF$^+$ are quite complex given the various couplings caused by the interaction of the thorium and fluorine atoms in ThF$^+$ along their respective degrees of freedom.
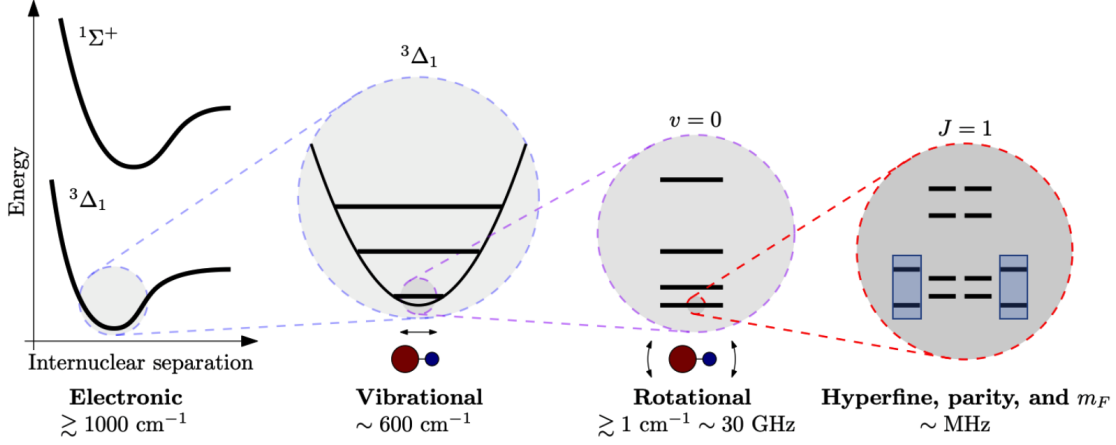
Figure 2.1: The quantum states of ThF$^+$, ranging from the large-scale Coulomb interaction between Th and F, through the ro-vibrational levels, and finally into its hyperfine states. Image credits: Kia Boon Ng.

The hyperfine interaction, depicted in the rightmost segment of figure 2.1, can only be fully resolved if one decouples the Zeeman and parity states by applying a rotating electric field (E_{rot}) and a rotating magnetic field (B_{rot}). Both of these fields apply perturbation Hamiltonians to the field free system, which in consequence induce a Stark shift and a Zeeman shift, respectively, onto the ions and their quantum states. Starting from the hyperfine structure, the Stark shift lifts some degeneracies among otherwise degenerate energy levels, whereas the Zeeman shift decouples degenerate energy states with different m_F quantum numbers which may otherwise share populations.

Within the J = 1, F = 3/2 block of the hyperfine Stark and Zeeman-shifted quantum energy states of ThF$^+$, there are a couple of transitions of interest that are sensitive to the value of the eEDM. These two transitions between the four states along the "upper" and "lower" doublets, with initial value of m_F = -3/2 and final

value of $m_F = 3/2$ and net $\Delta M = 3$, are referred to as the "science transitions" (figure 2.2). The frequency corresponding to the energy required to induce these transitions is called f_0, which is further explained in section 3.3.3. Without B_{rot} inducing the Zeeman Shift, f_0 would be near zero, making it hard to characterize any differences between the energy states in the upper and lower doublets. Hence, by applying B_{rot}, we obtain a more convenient f_0 of about 50 Hz.

Now, if the standard model prediction of the value of the eEDM is true, we shall see the transition between the two upper doublet states should have the same frequency as the two lower ones (f_0). However, if the real value of the eEDM is larger than the standard model prediction, then in the presence of a Zeeman shift-inducing static magnetic field these four states are separated by two distinct frequencies.
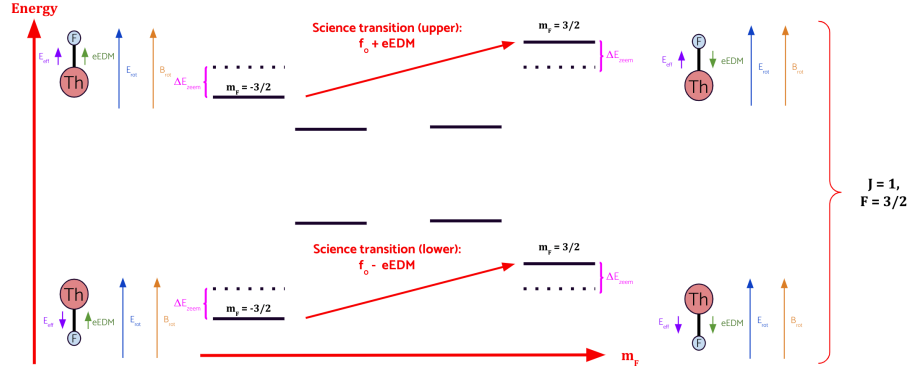
Figure 2.2: Considering that the energy corresponding to an individual state is of $E = \mu_B\, g_F\, m_F\, B_{rot}$, the energy derived from each science transition is $\Delta E = 3\, \mu_B\, g_F\, B_{rot}$ plus any eEDM contribution. The difference between these two science transitions isolates the signal of the eEDM.

Namely, after applying B_{rot} parallel to E_{rot} and biasing the desired energy states, we may experimentally find that the science transition is of 50 Hz + j μHz for the

upper doublet and 50 Hz - j μHz for the lower doublet, and this j μHz sub frequency is the isolated signal of the eEDM.

In the real experiment, we apply B_{rot} in a direction both parallel and anti-parallel to E_{rot}, obtain readings for the frequency corresponding to the eEDM in each case, and then average the results.

Therefore, these two science transitions are essential in our search to finding the eEDM, and finding a way to bias these two states away from $f_0 = 0$ via a Zeeman shift is essential to the experiment.

2.2   On shimming the Earth's magnetic field
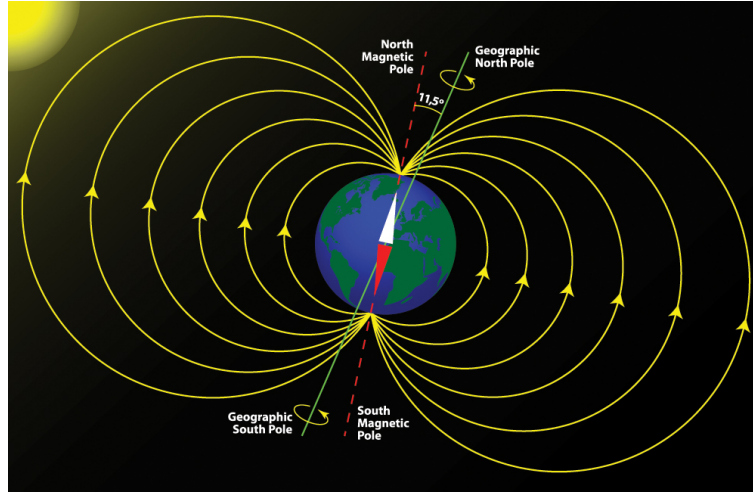
Figure 2.3: A visual representation of the magnetic field around the Earth's surface [6]

Due to its molten iron core, the Earth naturally produces a dipolar-like magnetic at all points along its surface (see figure 2.3). On the surface, the magnetic field lines tend to point and are strongest in the northbound direction, which is why artifacts

like compasses indicate to us the direction to the north pole given that their arrows align with the magnetic field lines. Despite the fact that the field lines are set to point north, they in reality have 3 dimensional properties, with significant contributions also pointing either east or west and either up (towards space) or down (into the Earth).

For example, using the NOAA magnetic field calculator, we can determine that the magnetic field is produced by the Earth at JILA (where the Generation III experiment will be housed) is of 20,613.8 nT north, 2,917.5 nT east, and 47,331.7 nT into the Earth. [5]

With regards to the eEDM generation III experiment, the Earth's magnetic field can be quite problematic given that it represents a source of stray magnetic field that may interfere with our measurement. As small as it may possibly be, having this stray magnetic field left unshimmed in an experiment that requires as much precision as ours is unacceptable.

Therefore, shimming out this potentially naturally-occurring yet potentially troublesome magnetic field is essential to the experiment.

3   Magnetic shim coils and their role in the overarching search for the eEDM in ThF$^+$ ions

As was mentioned in sections 2.1 and 2.2, finding a way to generate an f_0 to impose a Zeeman split on the ThF$^+$ ions is key to the experiment. This can be done a number of different ways, and the Bucket Brigade paper has listed different possible "plans"

to achieve this purpose.

The first of these plans, Plan A, is to generate B_{axgrad} through the means of a familiar method that was also used in generations I and II of the JILA eEDM experiment: by generating a static magnetic quadrupole around the ions via a set of Anti-Helmholtz coils. Here, B_{axgrad} is essentially the axial derivative of the magnetic field in the axial direction, or in other words (considering that $\hat{z}$ is generally used to refer to the axis of the trap in the generation III experiment):

$$B_{axgrad} = \frac{\partial B_z}{\partial z} \tag{3.1}$$

In addition to the above, it so happens that these coils can be used to cancel stray ambient magnetic field gradients coming from the environment, and one can also use Helmholtz coils in various configurations to shim out larger magnetic fields (such as the Earth's) as well as to impose a uniform magnetic field onto the ions if we so desire.

3.1   Scientific purpose for magnetic shim coils

In order to guarantee the desired long coherence time required for its Bucket Brigade setup to succeed and provide the desired results, the JILA EDM Generation III experiment needs to develop various sets of Helmholtz and Anti-Helmholtz coils and incorporate them into the current experimental setup. These coils and the respective magnetic fields they create when a current is applied thru them, have two main purposes: 1) to generate an axial magnetic field gradient (referred to as B_{axgrad}, with "axial" referring to the axis of the tube of the Generation III experiment's

multi-meter-long Paul trap) through which one can induce a Zeeman splitting to generate a desired science transition essential in finding the eEDM (more on that below) and 2) to "shim" out undesired ambient magnetic fields, be it from the Earth or any other stray source, which may cause noise in our measurements and cause problems in our setup if left unshimmed. Given that the Generation III team is currently in the process of testing the Baby Bucket, as opposed to the full Bucket Brigade, the magnetic field coils are being designed with the intent of being useful in the development and testing of the Baby Bucket and to understand its potential effectiveness within this simplified setup.

3.2   Magnetic coils and their various configurations

3.2.1   Single coil case

Running a current through a piece of wire generates a magnetic field which is azimuthal relative to the axis of the length of the wire. Via the Biot-Savart law, if one then wraps this piece of wire onto itself to create one or more "loops" in symmetrical shapes (most commonly in a circular shape) then the constructive and destructive superpositions between the contributions of the wire generating various magnetic fields end up generating a net magnetic field that is predominantly axial as seen by the figures below.
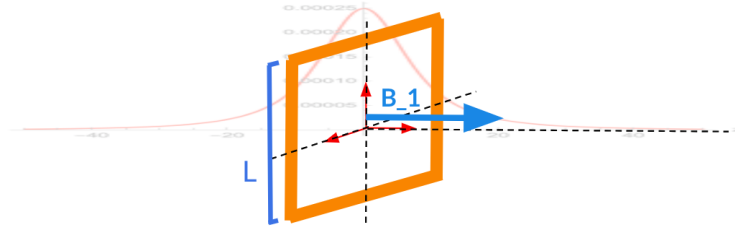
Figure 3.1: A visual representation of the magnetic field produced by a single coil of wire
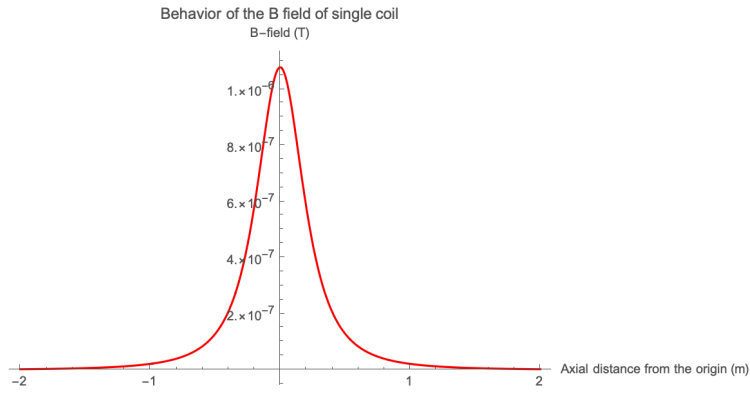
Figure 3.2: Plot of the magnetic behavior for a single coil of wire depicted in figure 3.1. (L = 20 inches, current = 1 amp, turns = 1)

The symmetry ends up working out very nicely when moving axially in one direction about the center of the single coil of wire, giving us the maximum possible magnetic field at the net center of the coiled wire and decreasing in magnitude when moving away from the net center in either direction.

3.2.2   Helmholtz pair

By taking two of these coils, placing them an arbitrary distance apart (typically referred to as "d"), and driving a current along the same direction in both coils (e.g:

both currents going clock-wise or both both currents going counter-clock-wise), one generates a Helmholtz pair of coils. The magnetic fields of these act in such a way that, moving axially in one direction, they add up to produce a characterizable non-zero magnetic field at the point directly between them with no first order gradient, as seen by the figures below.

Figure 3.3: A visual representation of the magnetic field produced by two loops of magnetic wire in Helmholtz configuration

Figure 3.4: Plot of the magnetic wire behavior for the Helmholtz set of coils depicted in figure 3.3. (For each coil: L = 20 inches, d = 19 inches, current = 1 amp, turns = 1)

3.2.3 Anti-Helmholtz pair

In contrast with the Helmholtz pair case, one can also take two coils, place them an arbitrary distance "d" apart, but this time driving a current in opposite directions for

each coil (e.g: one current going clock-wise and the other one going counter-clock-wise, or viceversa). In doing so, one generates what is called an Anti-Helmholtz pair of coils. The magnetic fields of these act in such a way that, moving axially in one direction, they perfectly cancel out at point directly between while having a characterizable non-zero, first order gradient, as seen by diagram.
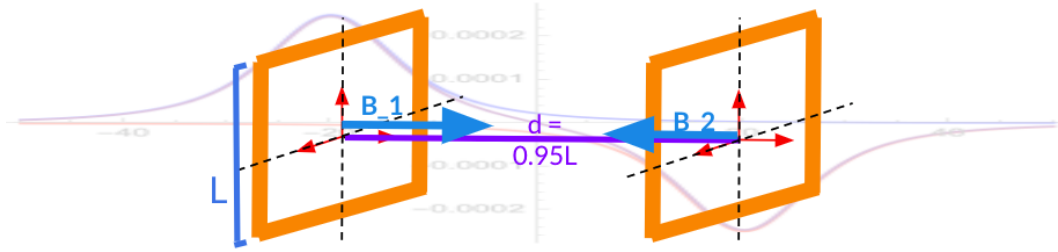
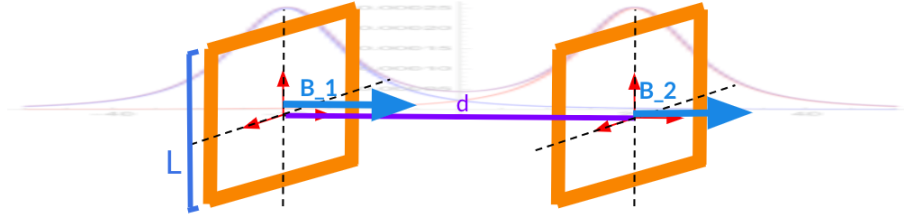Figure 3.5: A visual representation of the magnetic field produced by two loops of magnetic wire in Anti-Helmholtz configuration
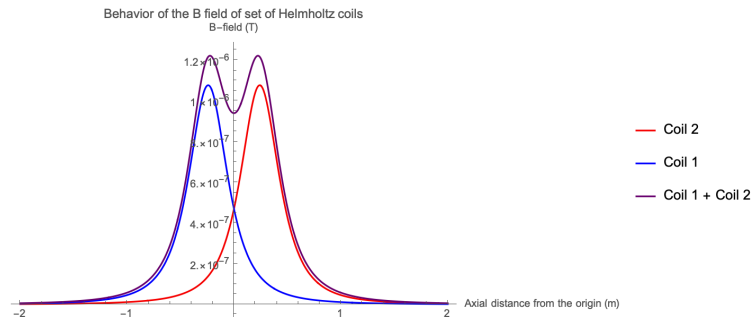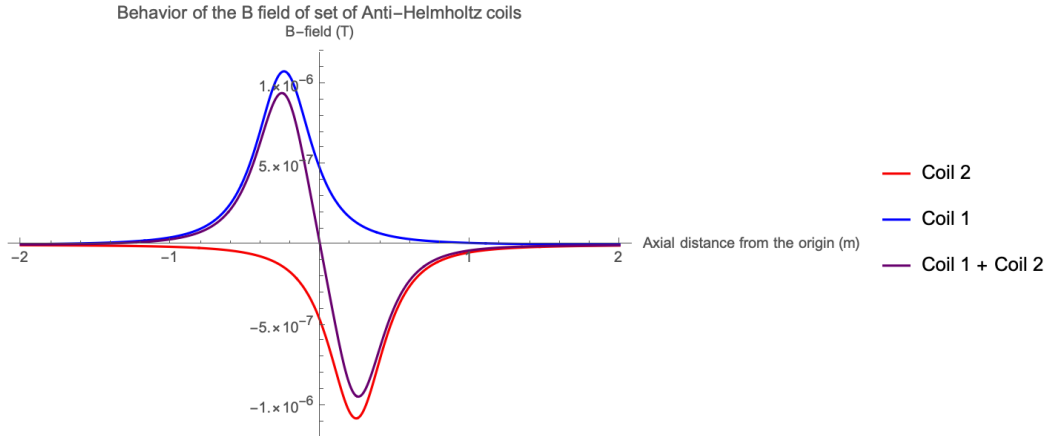

Figure 3.6: Plot of the magnetic wire behavior for the Anti-Helmholtz set of coils depicted in figure 3.5. (For each coil: L = 20 inches, d = 19 inches, current = 1 amp, turns = 1)

3.2.4   Disclaimer of use of Helmholtz and Anti-Helmholtz coils throughout this work compared to traditional conventions

When referring to the terms "Helmholtz coils" and "Anti-Helmholtz coils", researchers traditionally use these terms to refer almost exclusively to circular coils of radius R placed a distance R apart from one another, while following the same conventions on the currents described in sections 3.2.2 and 3.2.3. Throughout this work, however, we use these terms to more broadly describe coaxial coils in a parallel plane of varying radii, spacing and shape (circular, rectangular, square) with currents going in the same sense (Helmholtz) or the opposite sense (Anti-Helmholtz).

3.3   Anti-Helmholtz coils as a source of B_{axgrad} to generate Zeeman splitting

Given that our external magnetic field E_{rot} rotates periodically, the applied magnetic field must also rotate (which is reason for which we'll refer to it as B_{rot}) so that it points in a direction parallel or anti-parallel to the quantization axis E_{rot} generated by the electrodes to apply the desired Stark and Zeeman shifts at all times. In this subsection, we'll thoroughly describe the mechanism that relates B_{axgrad} to B_{rot} as generated by the Anti-Helmholtz coils and how both of these are related to the desired Zeeman splitting.

3.3.1   Relation between E_{rot} and the radius of micro-rotation r_{rot}

Within a plane orthogonal to the axis, and considering equation 1.1 for E_{rot}, the electric force exerted onto the ions from the electric field, F_{rot}, takes the form.

$$\vec{F_{rot}} = q_e \, \vec{E_{rot}} = q_e \, \epsilon_{rot} \begin{bmatrix} x \\ y \\ z = 0 \end{bmatrix} = q_e \, \epsilon_{rot} \begin{bmatrix} cos(\omega t) \\ sin(\omega t) \\ 0 \end{bmatrix} = m\ddot{\vec{r}} = ma \qquad (3.2)$$

Therefore, solving for $\ddot{\vec{r}}$, the acceleration, in the equation above yields:

$$\ddot{\vec{r}} = \frac{q_e \, \epsilon_{rot}}{m} \begin{bmatrix} cos(\omega t) \\ sin(\omega t) \\ 0 \end{bmatrix} \qquad (3.3)$$

And then integrating twice over $\ddot{\vec{r}}$ gives us $\vec{r_{rot}}$, the vector of rotation as defined in figure 3.9:

$$\vec{r_{rot}} = \int \int \ddot{\vec{r}} = -\frac{q_e \, \epsilon_{rot}}{m \, \omega^2} \begin{bmatrix} cos(\omega t) \\ sin(\omega t) \\ 0 \end{bmatrix} = -r_{rot} \, \frac{\vec{E_{rot}}}{\epsilon_{rot}} = -r_{rot} \, \hat{E_{rot}} \qquad (3.4)$$

where the scalar r_{rot} takes the value:

$$r_{rot} = \frac{q_e \, \epsilon_{rot}}{m \, \omega^2} \qquad (3.5)$$

With these definitions in mind, we can now make a geometry argument to justify the presence of a magnetic quadrupole.

3.3.2   Obtaining B_{rot} from B_{axgrad} via a magnetic quadrupole

Putting coils in Anti-Helmholtz configuration generates a magnetic quadrupole shaped magnetic field due to a given value of B_{axgrad}, which takes the form:

$$\vec{B}_{\text{from axgrad}} = \pm B_{axgrad} \begin{bmatrix} x \\ y \\ -2z \end{bmatrix} \tag{3.6}$$

This field, when viewed from the top, generates a 0-curl region onto its plane at z = 0 when viewed axially, which can be seen in figures 3.7 and 3.8. In both of these figures, the red circle represents the trace of a ThF$^+$ ion undergoing a circular micro rotation of radius r_{rot} due to E_{rot}, akin to figure 1.9. Notice that along this trajectory the ion always sees a magnetic field pointing radially outwards or inwards, hence always pointing in a direction parallel or anti-parallel to $\vec{E_{rot}}$.
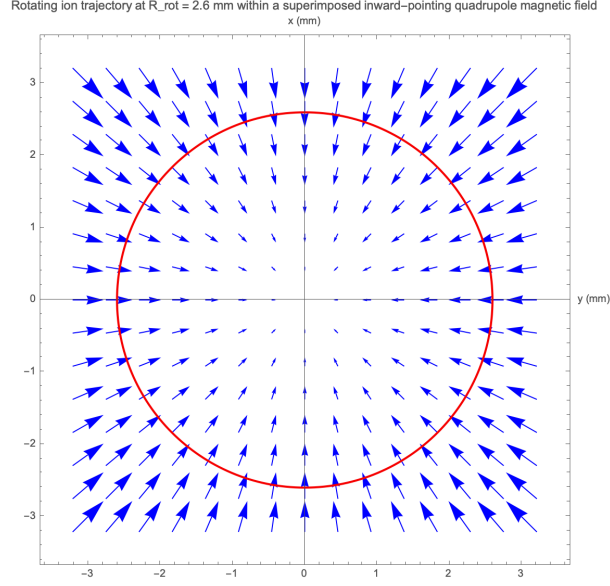
Figure 3.7: Quadrupole magnetic field for inward-facing $\vec{B} = -B_{axgrad}\cdot$ [x,y,0]^T
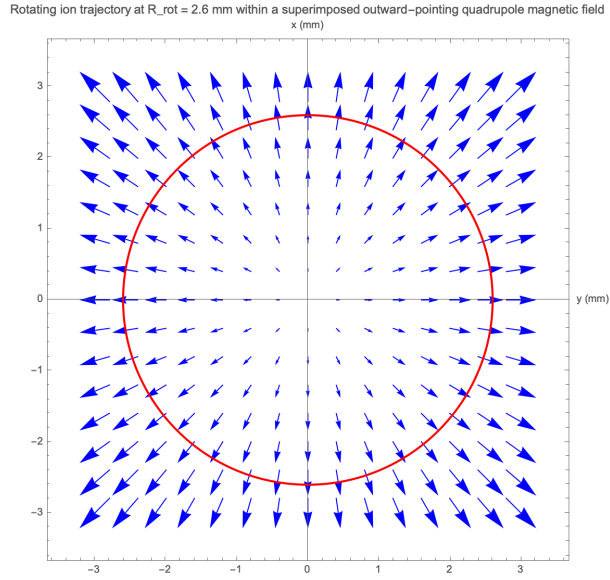
Figure 3.8: Quadrupole magnetic field for outward-facing $\vec{B} = +B_{axgrad}\cdot$ [x,y,0]^T

Now, think of an ion undergoing an E_{rot}-induced circular trajectory with radius

24

r_{rot} (as defined in equation 3.5) which we can describe through various vectors from

an arbitrary origin defined to be anywhere in space as seen in figure 3.9.
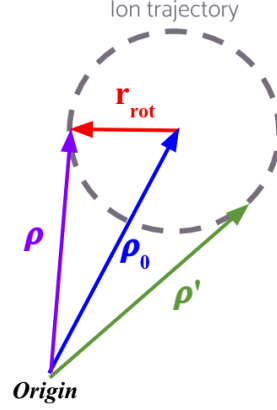
Figure 3.9: An ion's rotating trajectory induced by E_{rot} along the plane of the trap defined by three vectors, $\vec{r_{rot}}$, $\vec{\rho}$, and $\vec{\rho_0}$. ρ' is just meant to represent the net position vector at another position in time.

Via vector addition, we can see that, independent of our choice of origin, the

position vectors above are related by:

$$\vec{\rho}(t) = \vec{\rho_0} + \vec{r_{rot}}(t) \tag{3.7}$$

Analogously, we can similarly think of B_{rot} as a vector sum, always pointing

parallel or anti-parallel to E_{rot} as seen in figure 3.10.
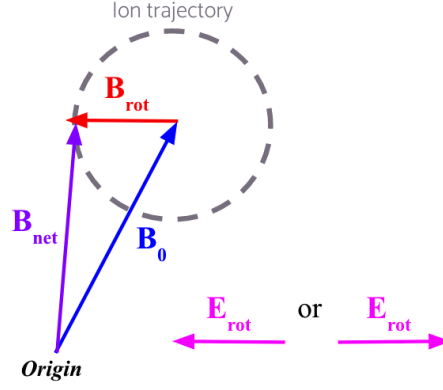
Figure 3.10: The magnetic field seen by the ions defined by three vectors, $\vec{B_{rot}}$, $\vec{B_{net}}$, and $\vec{B_0}$. $\vec{E_{rot}}$ is illustrated just to indicate that it shall be either in the parallel or the anti-parallel directions of $\vec{B_{rot}}$.

Via vector addition, we can see that, independent of our choice of origin, the magnetic field vectors above are related by:

$$\vec{B_{net}} = \vec{B_0} + \vec{B_{rot}}(t) \tag{3.8}$$

For the generic example in figure 3.10, we can redefine B_{net} in terms of B_{axgrad}. To do so, we can simplify equation 3.6 at z = 0 (the net center of the quadrupole, right in the middle point between the two coils in Anti-Helmholtz configuration, where ions will be located), also realizing that its components can be expressed as a function of equation 3.7. In the end, the expression simplifies to:

$$\vec{B}_{net}(t, x, y, z = 0) = B_{axgrad}\left(x\hat{x} + y\hat{y}\right) = B_{axgrad}\,\vec{\rho}(t) = B_{axgrad}(\vec{\rho_0} + \vec{r_{rot}}) \tag{3.9}$$

Considering the equation above, we can see that the amplitude of B_{rot} is just the

26

time averaged expression of the dot product between the already calculated B_{net} and $\hat{E}_{rot}$:

$$B_{rot} = \langle \vec{B}_{net}(\vec{\rho}(t)) \cdot \hat{E}_{rot} \rangle_t$$

$$= \langle B_{axgrad}(\vec{\rho_0} + \vec{r_{rot}}) \cdot \hat{E}_{rot} \rangle_t \tag{3.10}$$

$$= B_{axgrad}(\langle \vec{\rho_0} \cdot \hat{E}_{rot} \rangle_t + \langle \vec{r_{rot}} \cdot \hat{E}_{rot} \rangle_t)$$

Seeing that, over a full cycle $\left\langle \vec{\rho_0} \cdot \hat{E}_{rot} \right\rangle_t = 0$ (given $\vec{\rho_0}$ stays constant) that and $\left\langle \vec{r_{rot}} \cdot \hat{E}_{rot} \right\rangle_t = \pm r_{rot}$ (given that $\vec{r_{rot}}$ is always parallel or anti-parallel to $\hat{E}_{rot}$), equation 3.10 simplifies to:

$$B_{rot} = \pm B_{axgrad}\, r_{rot} \tag{3.11}$$

All of the above goes to show that, via a set of Anti-Helmholtz coils, one to induce a B_{rot} on an ion undergoing an E_{rot}-induced circular trajectory such that E_{rot} such that B_{rot} and E_{rot} always point in parallel or anti-parallel directions.

3.3.3 B_{rot} as a a source of f_0 and Zeeman splitting

Because of the presence of this magnetic field, an ion in this field will see a first-order Zeeman energy perturbation. Such perturbation takes the generic form:

$$U_{zeem} = -\vec{\mu_e} \cdot \vec{B_{rot}} \tag{3.12}$$

where, picking the good quantum number F which is conserved with time evolu-

tion, and considering that the value of Bohr magneton is $\mu_B = \frac{q_e\,\hbar}{2\,m}$:

$$\vec{\mu_e} = -\frac{g_f\,q_e}{2\,m}\,\vec{F} = -\frac{g\,\mu_B}{\hbar}\,\vec{F} \tag{3.13}$$

which makes equation 3.12 simplify to:

$$U_{zeem} = \frac{g_f\,\mu_B}{\hbar}\,\vec{F} \cdot \vec{B_{rot}} \tag{3.14}$$

Which is also referred to as the "magnetic energy" of the ions. Considering that B_{rot} always points along the quantization axis of the ThF$^+$ ions, the projection along its axis is just the quantum number m_F. Namely, $\langle \vec{F} \cdot \vec{B_{rot}} \rangle = m_F\,B_{rot}$. This allows for one final simplification for U_{zeem} in the form:

$$U_{zeem} = \frac{g_f\,\mu_B}{\hbar}\,m_F\,B_{rot} \tag{3.15}$$

With this in mind, the energy between the $m_F = \text{-}3/2$ and the $m_F = 3/2$ states depicted in figure 2.2 is just the difference between the final state and initial states when plugged into equation 3.15:

$$\Delta U_{zeem} = \Delta m\,g_f\,\mu_B\,B_{rot} = h\,f_0 \tag{3.16}$$

Knowing that, in scalar form, B_{rot}, B_{axgrad}, and r_{rot} are related by equation 3.11,

combining this with equation 3.16, and then solving for B_{axgrad} yields:

$$B_{axgrad} = \frac{h \, f_0 \, m_{ThF^+} \, \omega_{rot}^2}{q_e \, E_{rot} \, \Delta m \, g_f \, \mu_B} \tag{3.17}$$

Plugging in $h = 6.63 \times 10^{-34} \, \frac{J}{Hz}$, $f_0 = 50$ Hz, $m_{ThF^+} = 251 \, \frac{g}{mol} \cdot \frac{1}{6.022 \times 10^{23}} \frac{mol}{atom} \cdot 1 \times 10^{-3} \frac{kg}{g}$, $\omega_{rot} = 2\pi \cdot 150 \times 10^3$ Hz , $\Delta m = 3$, $g_f = 0.0149$, $\mu_B = 9.27 \times 10^{-24} \, \frac{J}{T}$, $E_{rot} = 60 \times 100 \, \frac{V}{m}$, and $q_e = -1.602 \times 10^{-19}$ C, and then we obtain that:

$$B_{axgrad} = 3.09 \times 10^{-5} \, \frac{T}{m} = 3.09 \, \frac{mG}{cm} \tag{3.18}$$

3.4   Helmholtz coil sets as a tool to shim out the Earth's magnetic field in three-dimensional space

In addition to the above, we are also interested in shimming out the magnetic field of the Earth which may also interfere with our measurement.

Compared to the elaborate calculations and derivations that were necessary to derive the first set of anti-Helmholtz coils, this is a relatively straightforward task. This is because the Earth's magnetic field, at any given location, is a constant three-dimensional vector with a minimal yearly deviation. This means that, to cancel it out, all we have to do is point an appropriate magnetic field of equal magnitude and opposite direction for all three directional axis.

We then remind ourselves of the properties for a set of magnetic coils in Helmholtz configuration located a certain distance apart, where the net magnetic field at the point exactly halfway between the coils is arbitrary and non-zero (in that one can

define it by carefully choosing the ampturns, nI, and size of the coils) with no first order gradient, as seen in section 3.2.2. This is extremely useful, as it means we can use this to our advantage to cancel out the magnetic field the way we desire.

4   Mathematical and physical definitions

It is now important to provide a few important mathematical and physical definitions, given that they will be very relevant throughout the rest of this paper.

Due to design-related motives that are thoroughly explained in section 5, all the coil pairs in this experiment have a square or rectangular symmetrical shape as opposed to the more commonly-used circular shaped coils. Hence, a special emphasis will be put in defining equations relevant to square coils throughout this section.

Given the complexity of these calculations, some of which end up yielding a few dozen lines worth of outputs, some of the final integrated results will not be cited on this paper.

4.1   Derivation of B across all space for rectangular coils

Starting with the most general case, and the non-idealized one where x,y,z $\neq$ 0, the following is the equation for the magnetic field of a single rectangular coil placed in the $\hat{x} - \hat{y}$ plane and centered at x=y=0, with sides equal to L_1 and L_2 driving a

current I (which can be positive or negative) along n number of turns:

$$B_{coil,rectangle}(x, y, z) =$$

$$\frac{\mu_0 n I}{4\pi} \left[\int_{-L_1/2}^{L_1/2} \frac{1}{[(x-l)^2 + (y-L_2/2)^2 + z^2]^{3/2}} \cdot \begin{bmatrix} 0 \\ -z \\ y - L_2/2 \end{bmatrix} \mathrm{d}l \right.$$

$$+ \int_{-L_2/2}^{L_2/2} \frac{1}{[(x-L_1/2)^2 + (y+l)^2 + z^2]^{3/2}} \cdot \begin{bmatrix} -z \\ 0 \\ x - L_1/2 \end{bmatrix} \mathrm{d}l \qquad (4.1)$$

$$+ \int_{-L_1/2}^{L_1/2} \frac{1}{[(x+l)^2 + (y+L_2/2)^2 + z^2]^{3/2}} \cdot \begin{bmatrix} 0 \\ z \\ -(y+L_2/2) \end{bmatrix} \mathrm{d}l$$

$$\left. + \int_{-L_2}^{L_2} \frac{1}{[(x+L_1/2)^2 + (y-l)^2 + z^2]^{3/2}} \cdot \begin{bmatrix} z \\ 0 \\ -(x+L_1/2) \end{bmatrix} \mathrm{d}l \right]$$

For a set of two coils, located an arbitrary distance d apart (i.e: located at z = $\pm\frac{d}{2}$), we need to add them together with the due offsets relative to the origin in $\hat{z}$. For Helmholtz coils, the signs of the addition of both segments must be both positive or negative, indicating that the current in both coils in the set points in the same direction:

$$B_{net,rectangle,Helmholtz}(x, y, z) =$$

$$B_{coil,rectangle}(x, y, z + \frac{d}{2}) + B_{coil,rectangle}(x, y, z - \frac{d}{2})$$

$$(4.2)$$

For anti-Helmholtz coils, the signs of the addition of each segments must be different (one positive, the other one negative), indicating that the current in each coils in the set points in opposite directions:

$$B_{net,rectangle,Helmholtz}(x,y,z) =$$
$$B_{coil,rectangle}(x,y,z+\frac{d}{2}) - B_{coil,rectangle}(x,y,z-\frac{d}{2}))$$

(4.3)

4.2   Derivation of B across all space for square coils

For the special case where $L_1 = L_2 = L$, for a single square coil, equation 4.1 simplifies to:

$$B_{coil,square}(x,y,z) =$$

$$\frac{\mu_0 n I}{4\pi} \left[\int_{-L/2}^{L/2} \frac{1}{[(x-l)^2 + (y-L/2)^2 + z^2]^{3/2}} \cdot (0, -z, (y-L/2)) \mathrm{d}l \right.$$

$$+ \int_{-L/2}^{L/2} \frac{1}{[(x-L/2)^2 + (y+l)^2 + z^2]^{3/2}} \cdot (-z, 0, (x-L/2)) \mathrm{d}l$$

$$+ \int_{-L/2}^{L/2} \frac{1}{[(x+l)^2 + (y+L/2)^2 + z^2]^{3/2}} \cdot (0, z, -(y+L/2)) \mathrm{d}l$$

$$\left. + \int_{-L/2}^{L/2} \frac{1}{[(x+L/2)^2 + (y-l)^2 + z^2]^{3/2}} \cdot (z, 0, -(x+L/2)) \mathrm{d}l \right]$$

(4.4)

For a set of two coils in Helmholtz configuration:

$$B_{square,Helmholtz}(x,y,z) =$$
$$B_{coil,square}(x,y,z+\frac{d}{2}) + B_{coil,square}(x,y,z-\frac{d}{2})$$

(4.5)

And for a set of two coils in anti-Helmholtz configuration:

$$B_{square,anti-Helmholtz}(x, y, z) =$$
$$B_{coil,square}(x, y, z + \frac{d}{2}) - B_{coil,square}(x, y, z - \frac{d}{2}) \tag{4.6}$$

4.3 Derivation of axial B for square coils

For the axial component of the B-field along $\hat{z}$ with $L_1 = L_2 = L$, where $x = y = 0$, equation 4.4 simplifies to:

$$B_z(x = 0, y = 0, z = z) = \frac{\mu_0 n I}{4\pi} \frac{8L^2}{\sqrt{\frac{L^2}{2} + z^2} \, (L^2 + 4z^2)} \tag{4.7}$$

For a set of two coils in Helmholtz configuration:

$$B_z(x = 0, y = 0, z = z) =$$
$$\frac{\mu_0 n I}{4\pi} \left[\frac{16L^2}{(d^2 + 4dz + L^2 + 4z^2)\sqrt{d^2 + 4dz + 2L^2 + 4z^2}} \right.$$
$$\left. + \frac{16L^2}{(d^2 - 4dz + L^2 + 4z^2)\sqrt{d^2 - 4dz + 2L^2 + 4z^2}} \right] \tag{4.8}$$

And for a set of two coils in anti-Helmholtz configuration:

$$B_z(x = 0, y = 0, z = z) =$$
$$\frac{\mu_0 n I}{4\pi} \left[\frac{16L^2}{(d^2 + 4dz + L^2 + 4z^2)\sqrt{d^2 + 4dz + 2L^2 + 4z^2}} \right.$$
$$\left. - \frac{16L^2}{(d^2 - 4dz + L^2 + 4z^2)\sqrt{d^2 - 4dz + 2L^2 + 4z^2}} \right] \tag{4.9}$$

4.4 Derivation of B_{axgrad} for Anti-Helmholtz square coils

The result from taking corresponding to equation 4.9, and considering that equation 3.1 which tells us to take the partial with respect to z of this expression to obtain the axial gradient, yield the expected result of B_{axgrad} at x = y = 0, z = z, which is:

$$B_{axgrad}(x = 0, y = 0, z = z) =$$

$$\frac{\mu_0 n I}{4\pi} \left[\frac{16L^2(8z - 4d)}{(d^2 - 4dz + L^2 + 4z^2)^2 \sqrt{d^2 - 4dz + 2L^2 + 4z^2}} \right.$$

$$- \frac{16L^2(4d + 8z)}{(d^2 + 4dz + L^2 + 4z^2)^2 \sqrt{d^2 + 4dz + 2L^2 + 4z^2}}$$

$$+ \frac{8L^2(8z - 4d)}{(d^2 - 4dz + L^2 + 4z^2)(d^2 - 4dz + 2L^2 + 4z^2)^{3/2}}$$

$$\left. - \frac{8L^2(4d + 8z)}{(d^2 + 4dz + L^2 + 4z^2)(d^2 + 4dz + 2L^2 + 4z^2)^{3/2}} \right]$$

(4.10)

4.4.1 Conventions used to refer to B_{axgrad} and its derivatives

Now is a good time to define some jargon which will come relevant in the following part of this paper, namely our definition B_{axgrad} and its derivatives.

Within the Taylor expansion of B_{axgrad} about the origin, $B_{axgrad,0}$ is defined to be the zeroth order term. Furthermore, and $B_{axgrad,1}$ is the first order term of this expansion, $B_{axgrad,2}$ the second, $B_{axgrad,3}$ the third, $B_{axgrad,4}$ fourth, and so on. In other words:

$$Taylor^4[\tilde{B}_{axgrad}(x, y, z)] =$$

$$B_{axgrad,0} + B_{axgrad,1} + B_{axgrad,2} + B_{axgrad,3} + B_{axgrad,4}$$

(4.11)

Where, for example, $B_{axgrad,2}$ equals:

$$B_{axgrad,2} = \frac{1}{2!}(x^2\partial_x^2\tilde{B}_{axgrad} + y^2\partial_y^2\tilde{B}_{axgrad} + z^2\partial_z^2\tilde{B}_{axgrad}$$
$$+2xy\partial_x\partial_y\tilde{B}_{axgrad} + 2xz\partial_x\partial_z\tilde{B}_{axgrad} + 2yz\partial_y\partial_z\tilde{B}_{axgrad}) \tag{4.12}$$

5   Design of the magnetic shim coils

A significant amount of time was spent carefully designing the coils, both in thought and in action, given the many relevant constraints set by both the experimental setup and the needs of the JILA eEDM generation III team.

5.1   Constraints and the reason behind square coils

In the current Baby Bucket setup our geometries are mostly rectangular and square due to the shapes of the setup that holds the vacuum chamber and the insulating foam around it. This can be appreciated in figure 5.1 below.

This geometrical constraint proves to be troublesome because it prevents us from building circular coils around the setup (which, in an ideal scenario, is preferred given that circular coils and their corresponding homogeneity are historically much more well-characterized). This is due to the potential interferences with both the surrounding cradle holding the tube and the optics, the optical table, and other elements that are going to be surrounding it in the final Baby Bucket setup. In short, an axially pointing circular setup does not fit our rather unusual geometries.
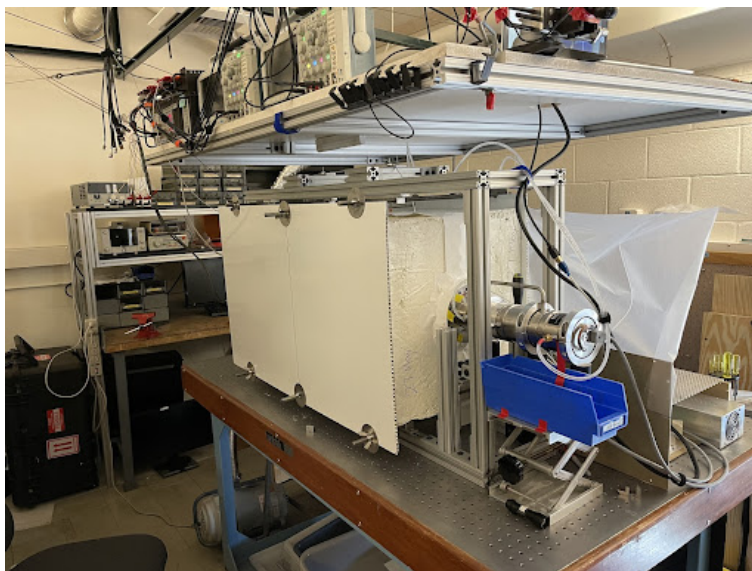
Figure 5.1: The current setup of the Baby Bucket. Note the mostly square and rectangular shapes created by the foam and the aluminum sheets pressing it together

With this issue in mind, it was decided that the coils will be square or rectangular as opposed to the traditional circular shape. While its homogeneity is less well-known and has to be theoretically characterized to see if it provides us with the uniformity we desire near the origin of the trap where the measurements will take place (see section 6 for this very uniformity analysis) it provides us with the convenience of being able to "mold" these coils so that they can comfortably fit around the Baby Bucket setup without interfering with anything nearby. Figure 5.2 elaborates on the pros and cons of doing a square versus a circular set of coils placed along the axis of the tube.
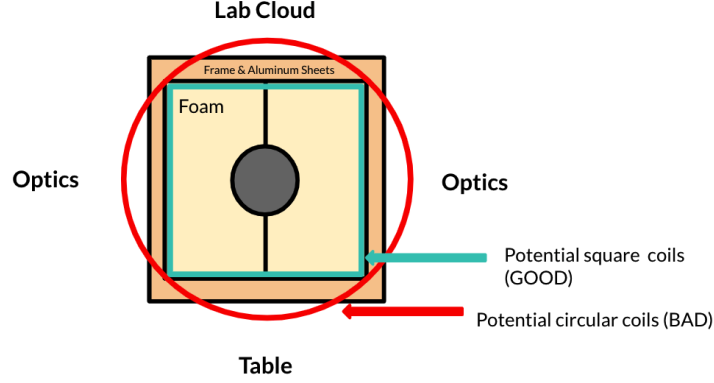
Figure 5.2: An abstract representation on how square and circle axial coils would fare up against one another based on the setup depicted in figure 5.1. It is clear that circular coils could not fit our rather limited space and would get in the way of the lab cloud, the optical table, and other objects surrounding the cryogenic insulation of the Bucket Brigade

5.2   Designing around the Taylor expansion of B_{axgrad}

As was said before, and as shown more visually by figure 5.3 below, one of the main objectives of the shimming coils is to be able to tune B_{axgrad} and minimize its corresponding higher order gradients. Taylor expanding the expression for B_{axgrad} generated by the Anti-Helmholtz coils along the z-hat direction (to 5 elements), we realize that all odd terms from the expansion result go to 0. A simple calculation where we set $B_{axgrad,2}$ equal to 0 and solve for d will allow us to see that $B_{axgrad,2}$ gets fully shimmed out as long as d/L = 0.95. However, recognizing that achieving this precise of a ratio may be too ideal, a theoretical error analysis must be done to characterize how "far" one can move from this ratio and still get a decent sized uniform zone (see section 6.3) per our desired requirements for the B_{axgrad}-generating Anti-Helmholtz coils. We're also very interested in the 5th order terms in the expansion,

37

$B_{axgrad,4}$, which cannot ever fully go to 0 unlike $B_{axgrad,2}$ above.

In order to minimize potential sources that may affect our desired coherence time, we have chosen that the valeue of the 4th element of the Taylor expansion divided by the 0th element must always be equal or smaller than 0.01 % (in our desired region in space, close to the net origin of the shimming coils where the ions are going to be located) to ensure that B_{axgrad} and its derivatives will minimally affect the coherence of the system and the ion cloud itself (see section 6.2).

The reason behind this 0.01 % number has to do with the fact that if f_0 is 50 Hz and we want coherence equal to 20 seconds, we see that a fractional uniformity of 2×10^{-4} will result in a final phase uniformity of about 1 radian. Since 2×10^{-4} is about 0.01 %, we have set this number as our bound.

$$\tilde{B}_{axgrad}(x, y, z) = \tilde{B}_{axgrad}(0,0,0)$$
$$+ x\partial_x\tilde{B}_{axgrad} + y\partial_y\tilde{B}_{axgrad} + z\partial_z\tilde{B}_{axgrad}$$
$$+ \frac{1}{2!}(x^2\partial_x^2\tilde{B}_{axgrad} + y^2\partial_y^2\tilde{B}_{axgrad} + z^2\partial_z^2\tilde{B}_{axgrad} + 2xy\partial_x\partial_y\tilde{B}_{axgrad} + 2xz\partial_x\partial_z\tilde{B}_{axgrad} + 2yz\partial_y\partial_z\tilde{B}_{axgrad})$$
$$+ (3^{\text{rd}} \text{ order terms})$$
$$+ (4^{\text{th}} \text{ order terms})$$

Goes to 0   Goes to 0, when d = 0.95 L   **These two do NOT go to 0.**

Goes to 0

Figure 5.3: This is the five term Taylor expansion of B_{axgrad} around the origin of the ion trap. Due to the nature of the expansion, the odd terms automatically go to 0 and the even terms do not go to 0. $B_{axgrad,2}$ becomes 0 as long as d/L = 0.95

It must be noted that, originally, the JILA EDM Generation III team intended on having 2 coupled sets of B_{axgrad} - related coils in order to independently control the first and the third derivatives of the net shimming B field with each coil. However, it has been found that there is no way (with the current symmetry) in which one would be able to control the first derivative with a set of shimming coils at all, given that solving for this condition shows us that d = 0 between a set of coils, which

is nonphysical. Instead, the focus has moved towards using a single set of coils minimizing the effect of the first derivative through the shimming fields from a single set of coupled Anti-Helmholtz coils.

5.3   Conventions on positions regarding the design

5.3.1   Use of $\hat{x}$, $\hat{y}$ $\hat{z}$ and relative to the positioning of the coils

The direction going along the axis of the tube of the Baby Bucket is generally referred to as the $\hat{z}$ direction, and the plane orthogonal to this axis is the $\hat{x} - \hat{y}$ plane, which is especially relevant to consider in sections 4 and 6, where important equations and theoretical analysis (respectively) are defined using these very conventions.

5.3.2   Use of NS, EW, and UD to describe the positioning of the coils

The Baby Bucket tube is loosely pointed along the North-South axis relative to the Earth, so sets of coils whose magnetic fields point predominantly along this axis ($\hat{z}$) are referred to as the North-South coils (NS or N-S, for short). In similar fashion, the coils whose magnetic fields point predominantly along East-West ($\hat{x}$) are referred to as the East-West coils (EW or E-W), and finally the coils that are pointing in the remaining axis ($\hat{y}$: up towards space, down towards the center of the Earth) are referred to as the Up-Down coils (UD or U-D). To distinguish it from NS (given that they're both placed along the same axis) and the rest of the coils, the anti-Helmholtz set of coils are referred to as "anti-Helmholtz coils" or "B_{axgrad} coils".

5.4   Needs and characterization of the geometries

As was hinted at before, the experiment needs 4 separate sets of coupled coils (meaning, two coils per set) built around this volume: one along the axis of the tube and foam in anti-Helmholtz configuration to generate B_{axgrad} and provide some ambient field protection, and then three in Helmholtz configuration to cancel out the Earth's magnetic field pointing along NS, EW, and UD.
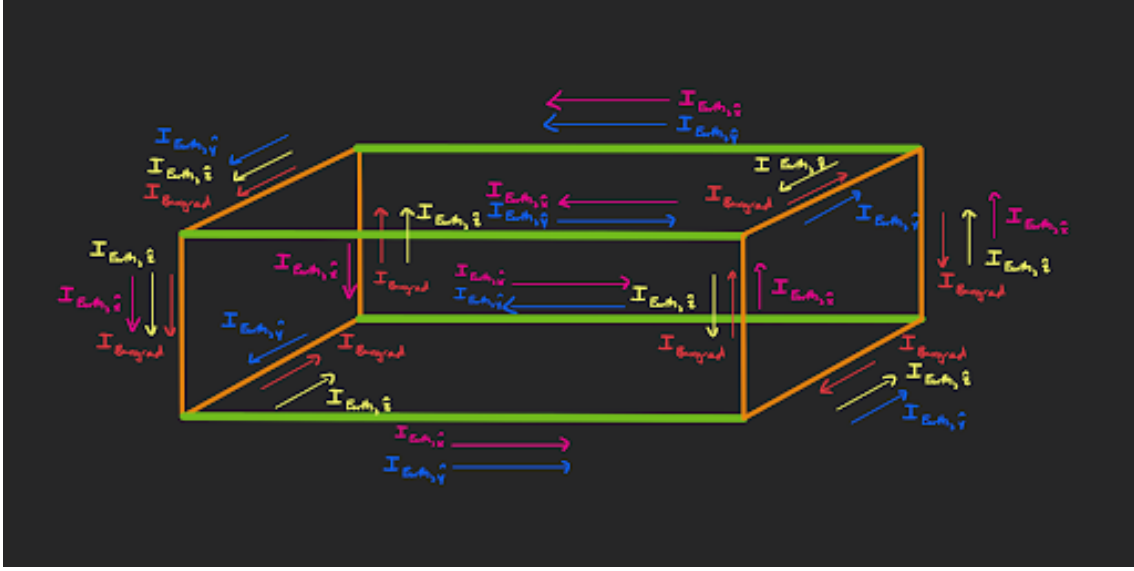
Figure 5.4: A sketch of all the different channels and currents that would be required in an assembled system with four coil pairs as described in this section.

One of the main design objectives was to have all these four sets of coils each be modular and easy to assemble and disassemble, given that the building schedule and methods behind the Baby Bucket and full Bucket Brigade experiments are highly volatile and complex, and may require relocations and multiple assemblies and disassemblies. Also, considering that some coils must be wound and partially assembled on site given the complex geometries of the setup, modularizing the setup also allows

for the possibility to have pre-wound coils (3 of the 6 total individual sets) which can be wound once in their square shapes and never have to be rewind them again into their square shapes.

Also, given that we want them to take as little space as possible within the assembly, all four sets of coils shall form a a compact "cube" of sorts, albeit with a 5 % difference in length between its axial direction and planar directions, when all of its modules are assembled together.

Given the geometries of the foam surrounding the bucket, it was decided that the axial set of NS and B_{axgrad} coils should have a length of 21 inches per side (L = 21 in) so that they better fit around the Bucket Brigade setup while giving us some room for leverage.

Considering that the separation between the Anti-Helmholtz coils must be $d = 0.95L$ as described in section 5.2, the final distance/separation between the B_{axgrad} coils ends up being $d = 19.95$ in.

For convenience and considering the materials being used, we need to have the NS coils be the largest and for the EW and UD coils to be a little smaller then such that they still form a near cube.

Hence, it was decided that:

1. The NS and B_{axgrad} coils shall be square and 21 x 21 inches on each side.

2. The EW coils shall each be square and 17.51 x 17.51 inches long on its sides

3. the UD coils shall be slightly rectangular, 17.51 x 16.51 inches long on its sides, given that it must fit in between the two sheets of aluminum holding the foam

as seen in figure 5.11.

5.5   Materials used for the design

5.5.1   Materials for the structure

Considering the geometries described above, the coils shall be built with cut-out segments of anodized aluminum U-channels throughout, which will serve as the means to wind long pieces of wire along their boundaries in repeated loops. Each coil has four of these pieces arranged such that they make up a square or rectangular shape, with the U shape pointing outwards, and the pieces are attached to each other via large corner brackets, and each individual coil is attached to its neighbors through small corner brackets.

5.5.2   Selection of wires based on reducing heat generation

The selection of magnetic wires was done thoughtfully because of the fact that a current running through a wire naturally produces power per:

$$P = I^2 R \tag{5.1}$$

Any power generated by the wires means that heat will be dissipated into its surroundings, which is important to consider given that the sets of coils are to be placed around the cryogenic insulation for the setup depicted in figure 5.1 (and as visualized by the CAD models in section 5.7).

The cold head and the cryogenic insulation are there to keep the Baby Bucket

tube as cold as possible, so it would be unwise for us to want to induce heat into said system via the coils.

Therefore, a thorough analysis was done to conservatively estimate the amount of heat that could be dissipated given: a) the total wire length needed for all sets of Helmholtz and Anti-Helmholtz coils, which is of about 11.2817 meters per turn for the Helmholtz sets added together and 4.2672 meters per turn for the anti-Helmholtz set alone, b) assuming that the number of ampturns for all the Helmholtz sets in NS, EW, and UD take up the value of largest of these 3 (which is UD at 29.148 ampturns, as calculated in section 5.6.2), and c) knowing that the number of ampturns required to generate the necessary B_{axgrad} is 3.336 ampturns, as determined in section 5.6.1.

We then had to do this analysis for various gauges of wire, given that the larger gauge at a fixed net length has a higher net resistance per length:

$$R_{net} = \rho \, \frac{L_{net}}{A_{cross-section,wire}} = \rho \, \frac{L_{net}}{\pi r_{wire}^2} = \rho \, \frac{n \, L_{\text{one turn}}}{\pi r_{wire}^2} \qquad (5.2)$$

Here ρ is the resistivity of the wire, L_{net} is the net length of a given wire, $A_{cross-section,wire}$ is the cross-sectional area of this wire (and r_{wire} is the radius of this cross-section), and n is the number of turns at a constant length per turn. In other words, the larger your gauge is at a constant length of total wire used and a constant number of ampturns, the smaller your net resistance will be, and the smaller the power dissipated will be. In addition to this, the larger the number of turns are at a constant number of ampturns and constant gauge, the smaller the net dissipated power will be.

Hence, combining the principles equations 5.1 and 5.2, we can study how the net power dissipated behaves as a function of the number of turns at a constant number of ampturns given the conditions above, setting 20 watts as an arbitrary upper bound for how much power we would like the coils to dissipate in a worst-case scenario.

Based on these parameters, the core goal is here is to a) determine a wire gauge to use for the coils and b) determine the number of turns to be used by the single Anti-Helmholtz set of coils and the four Helmholtz sets of coils.
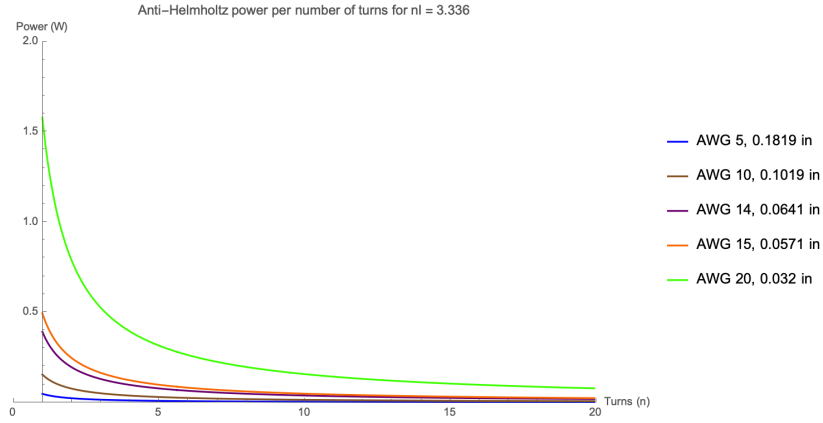

Figure 5.5: Power dissipated by the single Anti-Helmholtz coil set at a constant nI = 3.336. AWG refers to American Wire Gauge units, a standard in industry
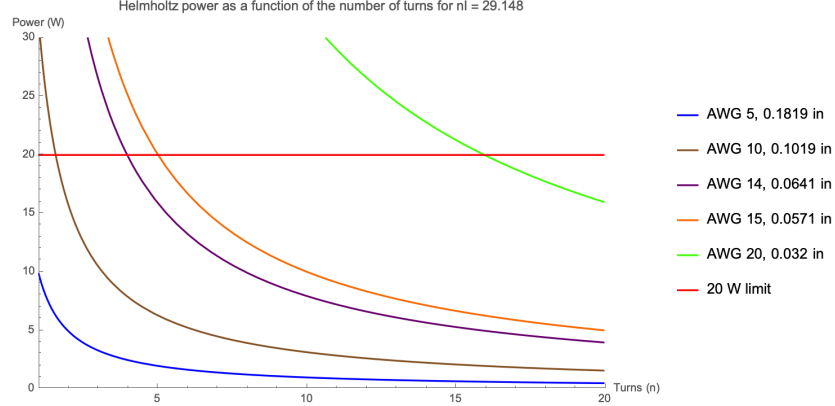
Figure 5.6: Power dissipated by the three Helmholtz coil sets together at a constant nI = 29.148
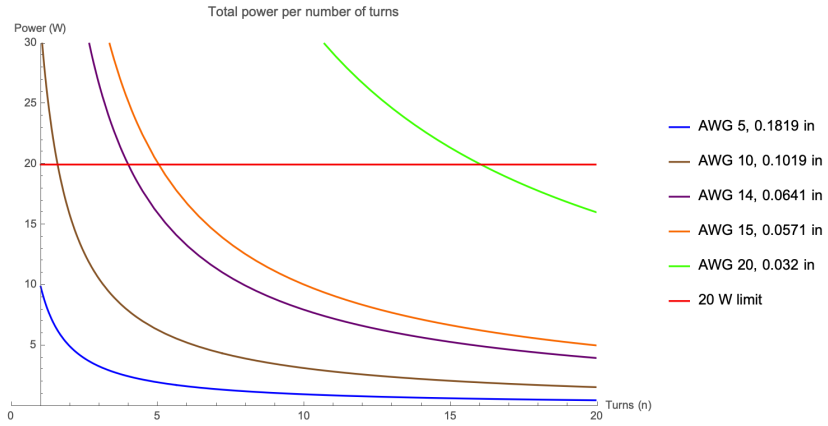
Figure 5.7: Total power dissipated by all the sets of coils together (addition of figures 5.5 with 5.6)

We can see from figures 5.5, 5.6, and 5.7 above that the Anti-Helmholtz set barely dissipates any power compared to the much greater amount dissipated by the addition of the four Helmholtz sets, and because of this the net addition of into figure 5.7 mostly reflects the power of the Helmholtz coils alone.

Given the results above and considering that relative to our upper bound of 20

W we aim to keep the power dissipation at least halfway below that of (10 W) and that a larger number of turns means a greater amount of labor required by any given lab member to wound these coils, we decided on using:

- AWG 14 wires at 10 turns for each of the three sets of Helmholtz coils

- AWG 14 wires at 3 turns for the single set of Anti-Helmholtz coils

5.6   Ampturns (nI) required for each set of coils

5.6.1   Calculation of ampturns (nI) needed to induce science transition with anti-Helmholtz coils

In designing the shimming coils, we were interested in knowing what number of ampturns (nI) we needed in order to get our desired B_{axgrad} from the anti-Helmholtz coils.

Per equation 3.18, $B_{axgrad} = 3.09\frac{mG}{cm} = 3.09x10^{-1}\frac{G}{m} = 3.09x10^{-5}\frac{T}{m}$. Therefore, calculating the number of ampturns can be done by letting B_{axgrad} equal this number and then solve for nI in equation 4.10, while letting z = 0 since we're interested in B_{axgrad} at the net origin where the ions are located.

$$3.09 \times 10^{-5} = \frac{\mu_0 nI}{2\pi}\left[\frac{16L^2(4d)}{\left(d^2+L^2\right)^2\sqrt{d^2+2L^2}} + \frac{8L^2(4d)}{\left(d^2+L^2\right)\left(d^2+2L^2\right)^{\frac{3}{2}}}\right] \quad (5.3)$$

$$nI = \frac{2\pi \cdot 3.09 \times 10^{-5}}{\mu_0\left[\frac{16L^2(4d)}{\left(d^2+L^2\right)^2\sqrt{d^2+2L^2}} + \frac{8L^2(4d)}{\left(d^2+L^2\right)\left(d^2+2L^2\right)^{\frac{3}{2}}}\right]} \quad (5.4)$$

46

And then plugging in $\mu_0 = 4\pi \times 10^{-7} \frac{H}{m}$ $d = 19.95$ in $= 0.50673$ m and $L = 21$ in $= 0.5334$ m.

$$nI = 3.336 \text{ ampturns} \tag{5.5}$$

5.6.2   Calculation of ampturns (nI) needed for shimming Helmholtz coils

As was mentioned before in section 2.2, we can tell what the magnetic field produced by the Earth at JILA in Boulder by using the NOAA magnetic field calculation tool [5], which tells us that the magnetic field produced by the Earth is of 20,613.8 nT north, 2,917.5 nT east, and 47,331.7 nT into the Earth. Therefore, one can perfectly cancel these fields from the Earth by inducing magnetic fields of equal magnitude and opposite direction with Helmholtz coils, pointing south with the NS coils, west with the EW coils, and "up" with the UD coils. We can then calculate the specific number of ampturns required to carry out these operations.

Given the geometries of the UD Helmholtz coils (17.51 in x 16.51 in per coil), the expression for its magnetic field simplifies to:

$$B_{\hat{y},UD,Helmholtz}(x=0, y=0, z=0) = \frac{\mu_0 nI}{4\pi} \cdot 16.2391 = 47,331.7 \text{ nT} \tag{5.6}$$

For EW, given its specific geometries (17.51 in x 17.51 in per coil):

$$B_{\hat{x},EW,Helmholtz}(x=0, y=0, z=0) = \frac{\mu_0 nI}{4\pi} \cdot 16.531 = 2,917.5 \text{ nT} \tag{5.7}$$

And for NS, given its specific geometries (21 in x 21 in per coil):

$$B_{\hat{z},NS,Helmholtz}(x=0, y=0, z=0) = \frac{\mu_0 nI}{4\pi} \cdot 17.3074 = 20,613.8 \text{ nT} \qquad (5.8)$$

And now solving for nI in each of these equations yields the necessary number of ampturns in each set:

- $nI_{south} = 11.9104$ ampturns

- $nI_{west} = 1.76$ ampturns

- $nI_{up} = 29.148$ ampturns

5.7   CAD Models

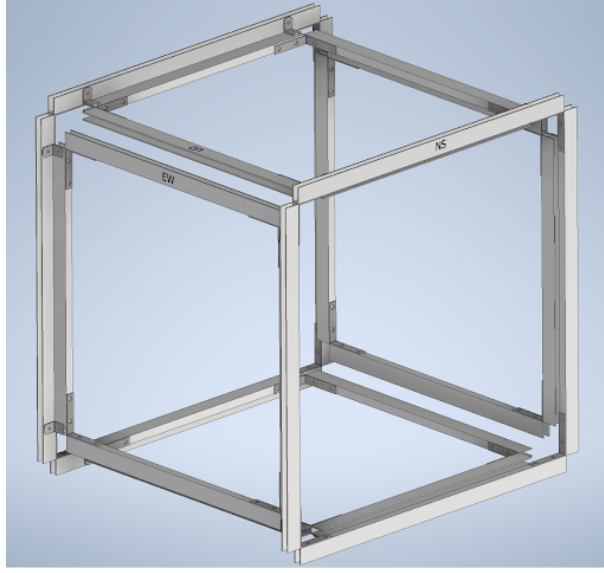Some CAD models of the setup designed and built can be found in the figures below.

Figure 5.8: A view of the setup of four sets of pairs of coils assembled together (note that NS and B_{axgrad} share the same channels in the figure)
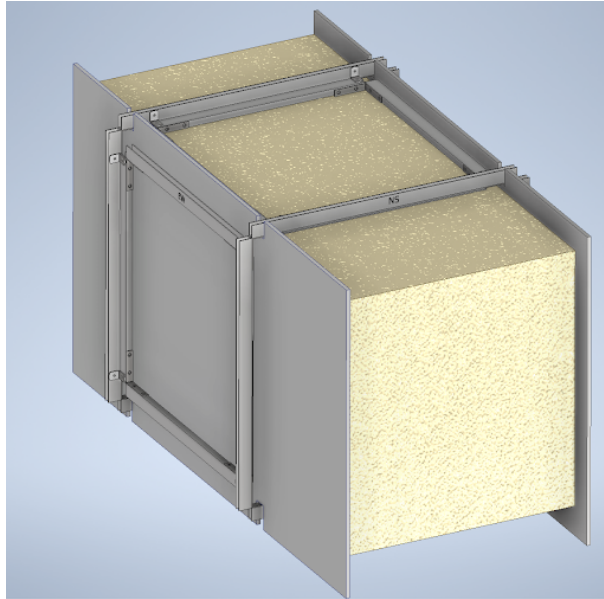
Figure 5.9: A view of how the setup depicted in figure 5.8 will fit around the foam insulation in figure 5.1

Figure 5.10: Figure 5.9, viewed from the side

Figure 5.11: Figure 5.9, viewed from the top

5.8   Building the coils and final product

Building the coils was an intense, multi-week job that required a significant amounts of effort to realize the project itself, especially given all the constraints and considerations that had to be considered based on the CAD model design as well as all the

other limitations cited in this paper. In the end, the final product that surged from these efforts ended up looking like the figure below:

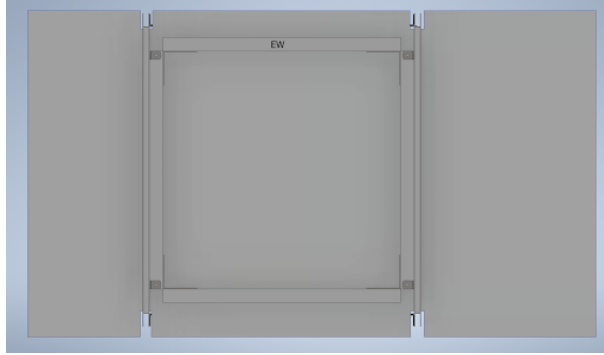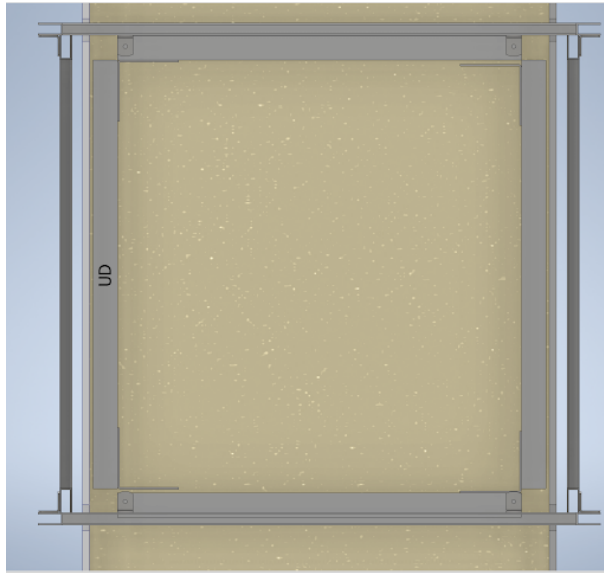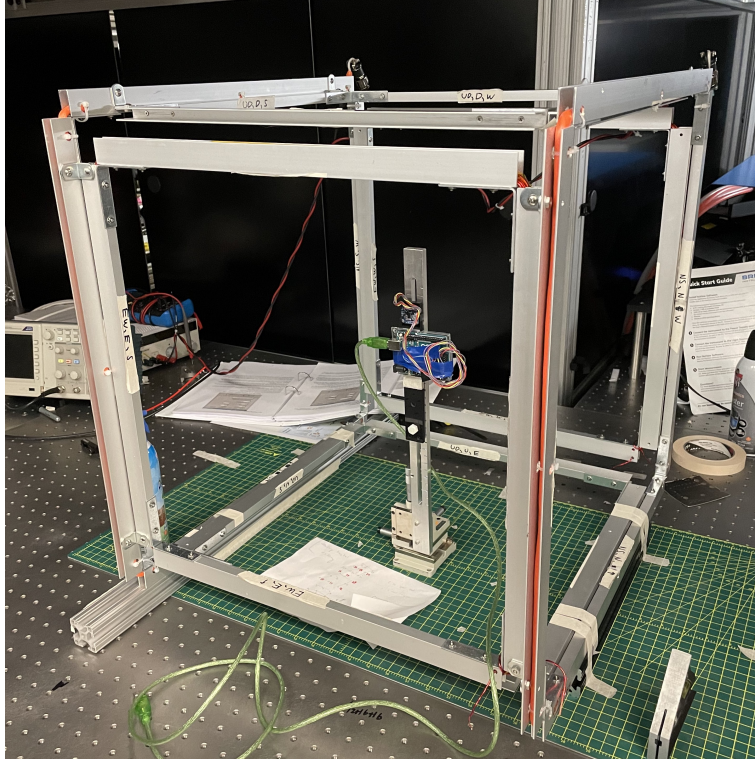Figure 5.12: Assembled structure for all the sets of coils. The orange three-threaded, 14 AWG wire used for the B_{axgrad} can be appreciated in the photo

6   Theoretical uniformity analysis to characterize decoherence arising from inhomogeneity in B_{axgrad}

The B_{axgrad}-generating anti-Helmholtz coils are of very special interest given that they generate the first order gradient that determines the frequency of the Zeeman shifted science transitions. Given our desire to eliminate any source of undesired

ambient magnetic field that may affect our measurement of the eEDM and the desired coherence time of the generation III experiment, higher order gradients of this B_{axgrad} can be extremely worrisome. Some of these are unavoidable due to the nature of the fields being generated and others can be caused by construction errors at the time of building the coils. To give a simple example: if when we are machining the coils some of them have different sizes to its sides, this will break the symmetry of the setup and cause decoherence. Unfortunately, due to the nature of manual labor, deviations from the ideal are to be expected in experimental physics, some of which are unavoidable even when having perfect constructions. Nevertheless, the question is not whether decoherence will exist, but rather to understand its scope and how much, and how well, we could work within these limits. Because of this, and given all the factors described above, one has to do a theoretical, Mathematica-based error analysis in order to determine how much "coherence", or lack thereof, can be found in the experimental setup for the Anti-Helmholtz coils to better understand its limitations and to determine if they give us a feasible region of uniformity given our desired parameters.

This problem can be separated into two parts:

1. Testing unavoidable inhomogeneity in $\frac{B_{axgrad,4}}{B_{axgrad,0}}$ from a perfect construction.

2. Testing additional inhomogeneity in $\frac{B_{axgrad,2}}{B_{axgrad,0}}$ from an imperfect construction.

These theoretical error analyses are based on parameters set by the Generation III team: wanting the ratios of and $\frac{B_{axgrad,2}}{B_{axgrad,0}}$ to be as minimal as possible, preferably on the order of less than 0.01 % or 0.02 % (as defined and explained in section 5.2).

6.1   Geometry of the size and micro rotation of the ThF$^+$ ion cloud

The ThF$^+$ molecules travel down the Bucket Brigade in the form of a roughly gaussian ion cloud. The Bucket Brigade paper anticipates:

$$r_{2\sigma} = 1 \text{ cm @ 30 K and } 2\pi \times 1 \text{ kHz}$$

$$r_{rot} = 2.60 \text{ mm @ 60 V/cm, 150 kHz}$$

$$r_{2\sigma} + r_{rot} = 1.26 \text{ cm}$$

Where $r_{2\sigma}$ is the radius of the ion cloud, r_{rot} is the radius of micro rotation of this ion cloud due to the induced E_{rot}, and $r_{2\sigma} + r_{rot}$ is the addition of these two.

In other words, any volume of good uniformity should be larger or equal to 1.26 cm in radius to acoomodate the entire volume taken up by the rotating ThF$^+$ cloud.

6.2   Characterization of inhomogeneity of $\frac{B_{axgrad,4}}{B_{axgrad,0}}$ under idealized behavior

After building the equation for $\frac{B_{axgrad,4}}{B_{axgrad,0}}$ in all space, we can probe it along 1) the x-y plane (z = 0), 2) y-z plane (x = 0), and 3) x-z plane (y = 0). The end result of these tests can be seen in the contour plots in the figures below. Within these, the light blue contours indicates the area where our desired inhomogeneity of 0.01 % or less is located. In light orange is the area where we have a inhomogeneity less or equal than 0.02 %, for reference. In yellow is a superimposed circle of radius = 2.032 cm, which is the radius of the so called area/volume of "uniformity". Below are all 3 figures:

53
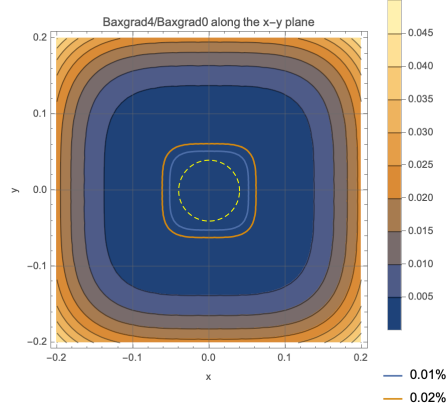
Figure 6.1: Plot of $B_{axgrad,4}/B_{axgrad,0}$ on the x-y plane at z = 0. Inside the region defined with the blue line is where $B_{axgrad,4}/B_{axgrad,0} \leq 0.1$ %, inside the orange region is where $B_{axgrad,4}/B_{axgrad,0} \leq 0.2$ % for reference, and the yellow dashed line is a circle of r = 0.04L $\approx$ 2.032 cm (assuming that the square coils' side is 20 inches long) for reference about the coherent area where the ion cloud could be within our desired region of tolerance considering all parameters and constraints. Axis values in figure are unit less length ($\frac{x}{L}$ and $\frac{y}{L}$).

Figure 6.2: Plot of $B_{axgrad,4}/B_{axgrad,0}$ on the y-z plane at z = 0. See description in figure 6.1. Axis values in figure are unit less length ($\frac{x}{L}$ and $\frac{y}{L}$).
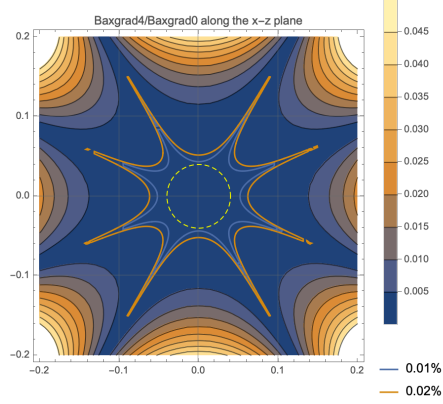
Figure 6.3: Plot of $B_{axgrad,4}/B_{axgrad,0}$ on the x-z plane at y = 0. See description in figure 6.1. Axis values in figure are unit less length ($\frac{x}{L}$ and $\frac{y}{L}$).

Moreover, combining the results from these 3 plots in a 3D model where we plot the homogeneity region equal or smaller to the same 0.01 % tolerance, we get the following results:
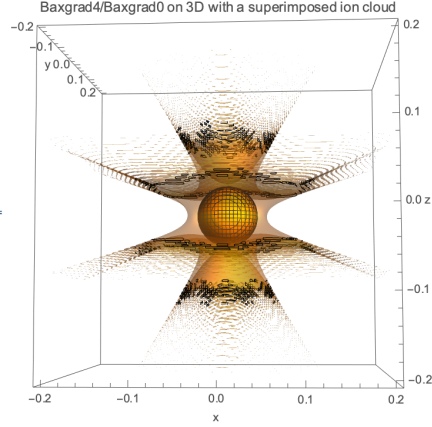
Figure 6.4: 3D plot of $B_{axgrad,4}/B_{axgrad,0}$ showing the desired region of tolerance of 0.01 % (viewed sideways). In the middle is a superimposed sphere of radius r = 2.032 cm to highlight the size 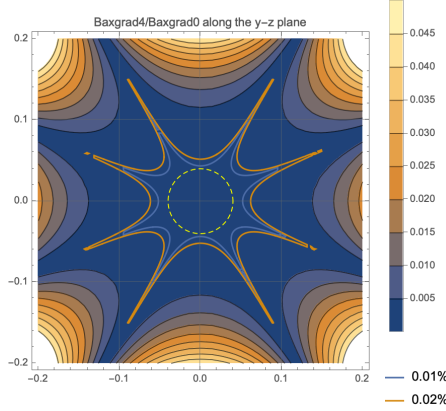of the so-called volume of uniformity. Axis values in figure are unit less length ($\frac{x}{L}$, $\frac{y}{L}$, and $\frac{z}{L}$).
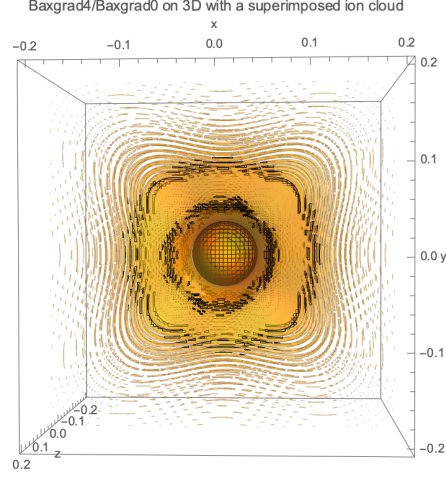
Figure 6.5: 3D plot of $B_{axgrad,4}/B_{axgrad,0}$ showing the desired region of tolerance of 0.01 % (viewed from the axis of the coils). Axis values in figure are unit less length $(\frac{x}{L}, \frac{y}{L},$ and $\frac{z}{L})$.

6.3   Characterization of inhomogeneity of $\frac{B_{axgrad,2}}{B_{axgrad,0}}$ subject to potential construction errors

As was mentioned before in section 5.2, $B_{axgrad,2}$ can vanish so long as the ratio of d/L is equal to 0.95. While convenient theoretically, it would be extremely challenging to replicate this exact result experimentally given all circumstances and sources of error that could mess up with this idealized ratio when building the setup. Hence, we perform an analysis to analyze how much potential sources of construction error can change a volume of homogeneity that is otherwise dominated by $\frac{B_{axgrad,4}}{B_{axgrad,0}}$ and then use these results to decide if, given the resulting radii of uniformity, the shimming coils are still even feasible to build despite these sources of error.

Using the exact same technique used for $\frac{B_{axgrad,4}}{B_{axgrad,0}}$ as depicted in figures 6.1, 6.2, and

56

6.3, the so-called coherent zones of $\frac{B_{axgrad,2}}{B_{axgrad,0}}$ are characterized by numerically solving

for the boundary conditions where a circular homogeneous radius (simulating our ion

cloud) can exist in all planes: x-y, y-z, and x-z. Considering the intent of providing

a thorough analysis of potential mishaps, a total of eleven specific cases of error were

studied, each representing a departure from the idealized case:

1. Both coils are offset in opposite directions, away from each other, by an equal
   distance from optimal d = 0.95L.

2. Both coils are offset in opposite directions, closer to each other, by an equal
   distance from optimal d = 0.95L.

3. A single coil is offset away from d = 0.95L by a certain distance.

4. A single coil is offset closer from d = 0.95L by a certain distance.

5. Both coils are offset in the same direction relative to the ion cloud (in any axial
   direction).

6. The size of the sides of the coils, L, increases in size.

7. The size of the sides of the coils, L, decreases in size.

8. Only one coil is rotated relative to the other, be it in y-z or x-z..

9. Both coils are rotated in the same or opposite directions, be it in y-z or x-z.

10. One coil is offset from the axis of the coils in any one direction in x-y relative
    to the other fixed coil.

11. The coils are anisotropic (one pair of sides of the coils is larger than the other
    pair by a certain length)

By studying all of these cases, the following extremes were identified. Refer to
the list above to identify each case number:

Error analysis of $\frac{B_{axgrad,2}}{B_{axgrad,0}}$		
Case number	Size of error	Radius of spherical coherent zone (cm)
1	1 cm	1.27542
2	0.9 cm	1.31135
3	1 cm	1.30801
4	0.8 cm	1.36589
5	1 cm	1.41648
6	0.5 cm	1.29271
7	0.5 cm	1.29602
8	14 degrees (5 cm axial offset)	3.97142
9	14 degrees (5 cm axial offset)	2.79443
10	0.5 cm	1.25911
11	1 cm	1.33896

6.4 Conclusions from theoretical analysis of $\frac{B_{axgrad,4}}{B_{axgrad,0}}$ and $\frac{B_{axgrad,2}}{B_{axgrad,0}}$

To say the least, it is good news that one can get a radius of uniformity in $\frac{B_{axgrad,4}}{B_{axgrad,0}}$ is equal to 2.032 cm (subject to a perfect construction) and that the the radii of uniformity of $\frac{B_{axgrad,2}}{B_{axgrad,0}}$ stays just above or about 1.26 cm (subject to various instances of imperfect construction). As was mentioned in section 6.1, the net radius of the rotating ion cloud $r_{2\sigma} + r_{rot}$ is equal to 1.26 cm, meaning that our tests indicate that we can have radii of uniformity that are large enough to just about enough to fit the entire rotating ion cloud. Therefore, the setup of Anti-Helmholtz coils is theoretically feasible and we can get the desired regions of uniformity as long as construction errors are kept within readily achievable tolerances as defined in the table from section 6.3.

7 Characterization and testing

Naturally, having the coils built meant that we have to do tests on them to see if they worked appropriately.

7.1 Characterization of the 3-axis magnetometer stick

An ADAFruit model LSM303DLHC seen below in figure 7.1 was chosen to be used used for nearly all the magnetic field testing surrounding this project. The magnetometer is a 3-axis Hall probe (with its axis labeled as $\hat{x}$, $\hat{y}$, and $\hat{z}$, which are unrelated to the conventions previously used to describe the design of the coils), meaning that it can measure magnetic fields in three dimensional space at any given

location, and it is powered by an Arduino Uno device with the appropriate code to allow the magnetometer to run.
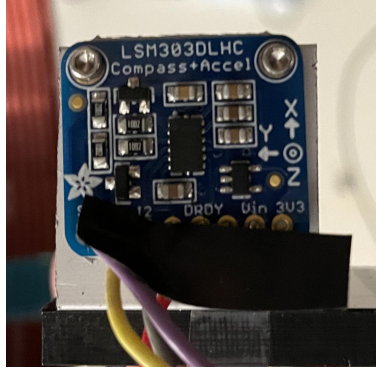
Figure 7.1: The ADAFruit model LSM303DLHC magnetometer

Early on, it was discovered that this very magnetometer had noticeable deviations in gain and DC offsets in all of three of its axis. Luckily, one can characterize these various gains and DC offsets by carrying on a series of experiments.

One can think of all possible sources of magnetic field as vector arrows adding up to one another in the frame of reference of the magnetometer (figure 7.2).
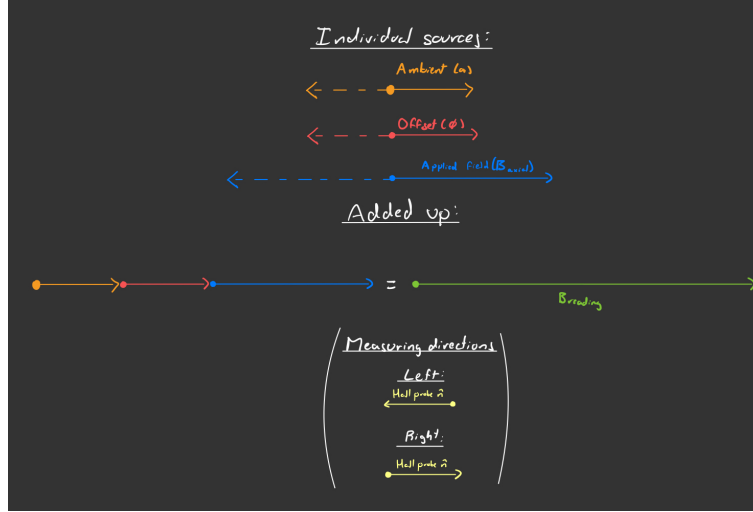
Figure 7.2: Visual depiction of the various different sources of magnetic field seen by the magnetometer, be it from ambient noise, a DC offset within the magnetometer itself, and the presence (or lack there of) coming from an applied external magnetic field. These axial fields can then be measured "left" and or "right" along the axis which they exist to yield different results

Therefore, we can use these traits of the fields to characterize the gains and offsets of a given magnetometer.

7.1.1 Magnetic field flip at a constant probe axis to characterize gain

If we let any given axis of the magnetometer remain still with an $\hat{n}$ along a constant axis and then we make two measurements, one with an applied external field pointing along $\hat{n}$ and the other with this external field pointing along -$\hat{n}$, we would see two readings:

$$B_{reading,1} = G\left(a + |B_{applied}|\right) + \phi$$

$$B_{reading,2} = G\left(a - |B_{applied}|\right) + \phi$$

Where $B_{reading,1}$ and $B_{reading,2}$ are the readings as described above, G is the gain, a is the ambient field (which ends up cancelling out later on, and hence doesn't need to be measured), ϕ is the DC offset, and $|B_{axial}|$ is the known value of the applied magnetic field.

If we then solve for ϕ in this system of equations and then make them equal to each other, while solving for the unknown G, we get:

$$B_{reading,1} - G\left(a + |B_{applied}|\right) = B_{reading,2} - G\left(a - |B_{applied}|\right)$$

$$2\,G\,|B_{applied}| = B_{reading,1} - B_{reading,2}$$

Which leads to the final equation for a gain calculated via a "magnetic field flip" setup.

$$G = \frac{B_{reading,1} - B_{reading,2}}{2\,|B_{applied}|} \tag{7.1}$$

7.1.2   Magnetometer axis flip at a constant applied magnetic field direction to characterize offsets

Now, if we now let the applied magnetic field remain constant in a direction $\hat{n}$ and then we physically flip the magnetometer to make make two measurements, one with a given axis of the magnetometer pointing along $\hat{n}$ and the other along -$\hat{n}$, we would see two readings.

$$B_{reading,1} = +G\left(a + |B_{applied}|\right) + \phi$$

$$B_{reading,2} = -G\left(a + |B_{applied}|\right) + \phi$$

Where the variables are the same as the ones defined in section 7.1.1.

If we then solve for $G\left(a + |B_{applied}|\right)$ in this system of equations and then make them equal to each other, while solving for the unknown ϕ, we get:

$$B_{reading,1} - \phi = -B_{reading,2} + \phi$$

Which leads to the final equation for a gain calculated via a "magnetometer flip" setup.

$$\phi = \frac{B_{reading,1} + B_{reading,2}}{2} \tag{7.2}$$

Figure 7.3: One of the setups used to test the gain of the and offsets of the magne-
tometer using the JILA eEDM generation I coils

7.1.3   Results

Results of gain and offset analysis		
Axis	DC offset (uT)	Gain
x	7.0375	0.9922
y	-6.15	0.9920
z	2.21	1.0924

64

Plot of theoretical axial magnetic field expectation in Gen 1 coils with real measured values in 3−axis magnetometer

B−field (uT)

- 2 amps (theory)
- 1.97 amps (theory)
- Measured X values
- Measured Y values
- Measured Z values
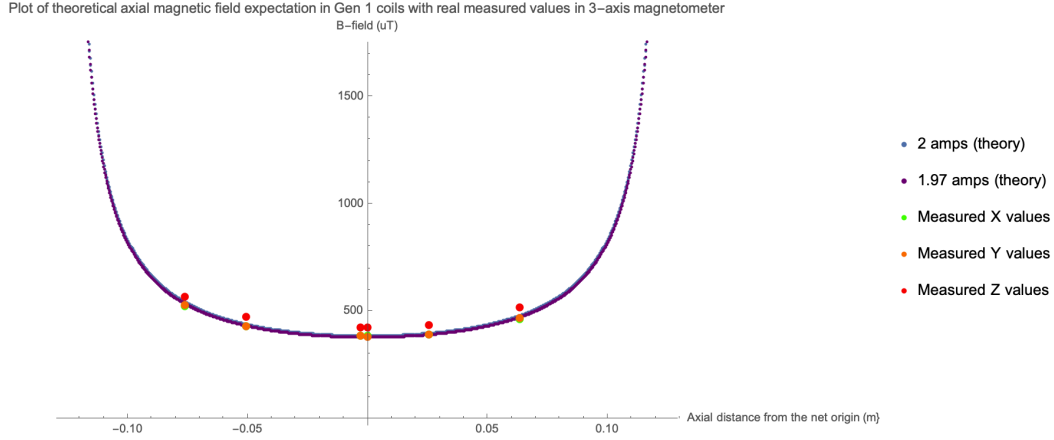
Axial distance from the net origin (m)

Figure 7.4: A plot of comparing some experimentally measured values of the magnetic field along the vertical axis of one of the JILA eEDM generation I coils at a constant current (using all three channels of the magnetometer, $\hat{x}$, $\hat{y}$, and $\hat{z}$) compared with the theoretical expectation. It is clear that there is some anomalous gain in the $\hat{z}$ axis relative to $\hat{x}$ and $\hat{y}$ (the $\hat{x}$ values are pretty much overlapping to those of $\hat{y}$

7.2   Plan to take data to test homogeneity generated by B_{axgrad} coils

It is necessary to test whether the anti-Helmholtz coils in our setup yield the necessary B_{axgrad} and fractional uniformity in a real experimental environment. Unfortunately, due to time constraints, it won't be possible to do these tests as part of this thesis. Nevertheless, we'll proceed to describe the proceedure to test the set.

After installing the B_{axgrad} coils and their wires in place and considering the three turns in them, a current of 1.112 amps should run thru the wires (both which combined correspond to the nI = 3.336 ampturns calculated in equation 5.5).

Then, the magnetic field and the gradients should be tested in the following way. As depicted by figure 7.5, the magnetic field and the gradients generated by the coils

shall tested in a 27 point grid about the net center (the "origin", or x=y=z=0 as defined in this work) of system of anti-Helmholtz coils, with the distancing between each of these individual points being of 10 cm vertically and/or horizontally.
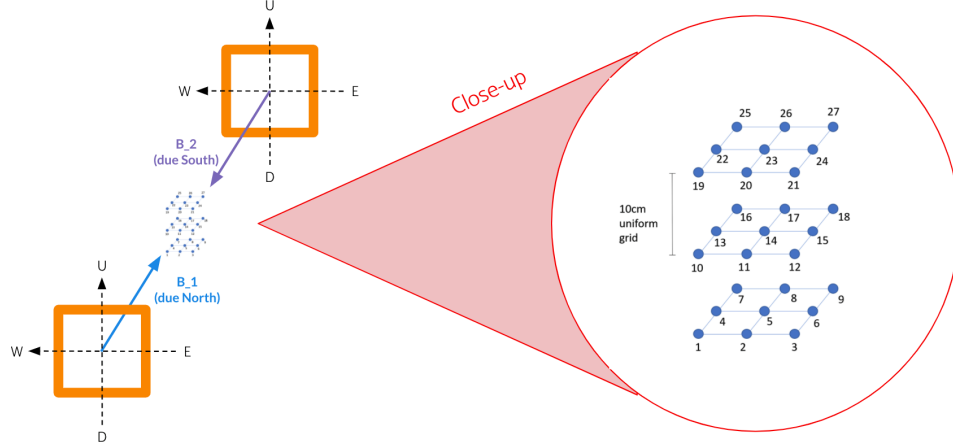

Figure 7.5: A depiction of the B_{axgrad} "grid" along which they shall be tested. Point number 14 is at the dead-center of the coils (x=y=z=0) and all points are separated by 10 cm vertically and/or horizontally in three dimensional space

We will fit the data from this finite mesh to the multipole expansion of the magnetic field up to $Y_l^m(\theta, \phi)$ spherical harmonic terms of $l = 4$ that correspond to the second derivative of B_{axgrad} ($\frac{\partial^2 B_{axgrad}}{\partial x^2}$, $\frac{\partial^2 B_{axgrad}}{\partial y^2}$, and $\frac{\partial^2 B_{axgrad}}{\partial z^2}$) and use this to predict field uniformity over a sphere of radius 1.26 cm (defined to be $r_{2\sigma} + r_{rot}$ in section 6.1) at the center of the trap. Data should taken in two environments: oe top of the optical table and on top of a wooden table. This is because the optical table on which the Bucket Brigade is going to be assembled on was discovered to be highly magnetic and with intense gradients in three-dimensional space, reason for which we want to test the coils in both highly magnetic and non-magnetic environments.

8   Conclusions

Theoretically, square magnetic shim coils in anti-Helmholtz configuration can be built such that they generate a desired B_{axgrad} to generate a desired Zeeman splitting corresponding to a set value of $f_0 = 50$ Hz to induce the science transition onto the upper and lower doublets within the E_{rot}-induced, Stark shifted hyper fine structure of ThF^+.

Via thorough analysis, while sticking to set boundaries of fractional homogeneity of 0.01% or less in both $\frac{B_{axgrad,4}}{B_{axgrad,0}}$ (for a perfect construction) and $\frac{B_{axgrad,2}}{B_{axgrad,0}}$ (for an imperfect construction), we can ensure that this set of anti-Helmholtz coil is not a significant source of fractional inhomogeneity that could prevent the ThF^+ ions from reaching their desired 20 second coherence times.

In addition to the above, one can use square Helmholtz coils to shim out the Earth's magnetic field in three-dimensional space and also be able to provide a large, arbitrary magnetic field onto the ions if need be, which is the reason for which onto the design of the pseudo-"cube" structure encompassing three sets of Helmholtz coils and one set of axial anti-Helmholtz coils.

It was proven that all of this can be done by designing a setup that can be tailor-fit around the unusual geometries of the JILA eEDM generation III Baby Bucket setup, while allowing for the setup to be easy to assemble and disassemble. Given that the coils are to be placed about the cryogenically-insulated section of the Baby Bucket, the setup was designed such that they always dissipate 10 W or less onto its surroundings.

Experimentally, once the coils were built, they shall be tested to see if they provide

the necessary fractional homogeneity and B_{axgrad} required by the experiment, work which is beyond the scope of this thesis. Moreover, once the JILA eEDM generation III collaboration has prepared the entire "Baby Bucket" setup and is ready to "see" ions in order to test their coherence times, future work regarding this project shall focus in studying the behavior of the ions under the influence or lack thereof of the B_{axgrad} generated by the Anti-Helmholtz coils and the shimming generated by the Helmholtz coils.

9   References

[1]   William B. Cairncross et al. "Precision Measurement of the Electron's Electric Dipole Moment Using Trapped Molecular Ions". In: *Physical Review Letters* 119.15 (Oct. 2017). ISSN: 1079-7114. DOI: 10.1103/physrevlett.119.153001. URL: http://dx.doi.org/10.1103/PhysRevLett.119.153001.

[2]   Yan Zhou et al. "Visible and ultraviolet laser spectroscopy of ThF". In: *Journal of Molecular Spectroscopy* 358 (2019), pp. 1–16.

[3]   CERN. *The Standard Model.* 2022. URL: https://home.cern/science/physics/standard-model (visited on 02/02/2022).

[4]   Kia Boon Ng et al. "Spectroscopy on the eEDM-sensitive states of ThF$^+$". In: (2022). arXiv: 2202.01346 [physics.atom-ph].

[5]   NOAA. *NOAA Magnetic Field calculator.* 2022. URL: https://www.ngdc.noaa.gov/geomag/calculators/magcalc.shtml (visited on 03/02/2022).

[6]   ShutterStock. *Illustration of the Earth's magnetic field.* 2022. URL: https://www.shutterstock.com/image-vector/magnetic-geographical-pole-earth-106154861 (visited on 03/05/2022).